DOKUZ EYLÜL UNIVERSITY
GRADUATE SCHOOL OF NATURAL AND APPLIED SCIENCES

IMPROVEMENT OF PARTICLE IMAGE VELOCIMETRY

by

Ceyda GÜNAY

September, 2020

İZMİR

IMPROVEMENT OF PARTICLE IMAGE VELOCIMETRY

A Thesis Submitted to the
Graduate School of Natural and Applied Sciences of Dokuz Eylül University
In Partial Fulfillment of the Requirements for the Degree of Master of Science
in Mechanical Engineering, Energy Program

by

Ceyda GÜNAY

September, 2020

İZMİR

M.Sc THESIS EXAMINATION RESULT FORM

We have read the thesis entitled **"IMPROVEMENT OF PARTICLE IMAGE VELOCIMETRY"** completed by **CEYDA GÜNAY** under supervision of **PROF. DR. DİLEK KUMLUTAŞ** and we certify that in our opinion it is fully adequate, in scope and in quality, as a thesis for the degree of Master of Science.

Prof. Dr. Dilek KUMLUTAŞ

Supervisor

Prof. Dr. Can Özgür ÇOLPAN

(Jury Member)

Doç. Dr. Mustafa Turhan ÇOBAN

(Jury Member)

Prof.Dr. Özgür ÖZÇELİK

Director
Graduate School of Natural and Applied Sciences

ACKNOWLEDGMENT

Before all the sentences to be said, I would like to thank my supervisor Prof. Dr. Dilek KUMLUTAŞ with all my heart. I am very grateful for the way she has guided me with all her sincere ideas.

I would like to thank Dr. Özgün ÖZER for sharing his knowledge about experiments with me. I am proud of working with him as a student because he teaches me to gain a different point of view with his lectures about photography. In addition, I would like to thank M. Sc. Utku Alp YÜCEKAYA for times we work together.

I would like to express my sincere thanks to my friends Cansu USLU and Yeliz KORU who have embellished my difficult times with their support and warm smiles.

Most importantly, I would like to thank my mother Gülbahar ALGÖL for her endless support and trust in me. Frankly, without the things she taught me, I wouldn't have found my way.

Ceyda GÜNAY

IMPROVEMENT OF PARTICLE IMAGE VELOCIMETRY

ABSTRACT

The aim of this study is to determine the aerodynamic characteristics of electric vehicles with Particle Image Velocimetry (PIV) and Computational Fluid Dynamics (CFD). In this sense, the parameters that vary according to the flow and flow structure to be formed around the vehicle were examined.

Within the scope of this study, the electric vehicles were modeled on a certain scale. These models were prepared for experimental study with three-dimensional printer. Particle Image Velocimetry (PIV) experiments were conducted in the wind tunnel, which prepared for providing the flow domain around the vehicles. In addition, the three dimensional numerical models of the vehicles were created by using commercial software ANSYS Fluent. The velocity and velocity-related characteristics obtained from these models, which were created by using CFD method, were compared with the data obtained from the PIV experiments. The coherence of the experimental and numerical results was evaluated. This evaluation provided validation to analyze numerically. The effects of different geometric design parameters on velocity maps and flow separations were investigated and compared. Numerical analysis of different velocities acting on the electric vehicle geometries were carried out and the effect of different parameters on the flow region was compared. Also, the effects of different turbulence models on the accuracy were investigated. According to the obtained results, parameters which minimize the aerodynamic forces on the vehicle were determined.

Keywords: Particle image velocimetry (PIV), computational fluid dynamics (CFD), aerodynamics of road vehicle, flow separations

PARÇACIK GÖRÜNTÜLEMELİ HIZ ÖLÇÜMÜ YÖNTEMİNİN GELİŞTİRİLMESİ

ÖZ

Bu çalışmanın amacı elektrikli araçlar üzerindeki aerodinamik karakteristiklerin belirlenmesidir. Bu anlamda araçların çevresinde oluşacak akış ve akışa bağlı parametreler irdelenmiştir.

Bu çalışma kapsamında elektrikli araçlar belirli ölçekte küçültülerek modellenmiştir. Elde edilen bu modeller üç boyutlu yazıcı ile deneysel çalışmaya hazır hale getirilmiştir. Araç çevresi akış ortamını sağlamak amacıyla hazırlanan rüzgar tünelinde Parçacık Görüntülemeli Hız Ölçümü (PGHÖ) deneyleri yapılmıştır. Bu deneylerden aracın aerodinamik olarak incelenmesinde kullanılan hız dağılımı ve akış ayrılmaları yapıları elde edilmiştir. Ayrıca araçların nümerik modelleri, ticari bir yazılım olan ANSYS Fluent paket programı kullanılarak üç boyutlu olarak oluşturulmuştur. Hesaplamalı Akışkanlar Dinamiği (HAD) yöntemi kullanılarak oluşturulan bu modelden elde edilen hız ve hıza bağlı karakteristikler PGHÖ deneylerinden elde edilen verilerle karşılaştırılmıştır. Sayısal ve deneysel çalışmalardan elde edilen sonuçlar arasındaki uyum değerlendirilmiştir. Bu değerlendirme farklı akış bölgesi parametrelerinin kullanıldığı sayısal analizler için doğrulama sağlamıştır. Farklı geometrik tasarımların ve hız değerlerinin akış ayrılmalarına ve hız haritalarına olan etkisi irdelenmiş ve karşılaştırılmıştır. Ayrıca kullanılan türbülans modellerinin çözüm hassasiyetine olan etkisi de incelenmiştir. Elde edilen sonuçlar doğrultusunda araç üzerine etkiyen aerodinamik kuvvetleri en aza indiren parametreler sunulmuştur.

Anahtar Kelimeler: Parçacık görüntülemeli hız ölçümü yöntemi (PGHÖ), hesaplamalı akışkanlar dinamiği (HAD), araç aerodinamiği, akış ayrılmaları

CONTENTS

Page

LIST OF FIGURES

Page

LIST OF TABLES

Page

CHAPTER ONE
INTRODUCTION

1.1 Introduction

Automotive companies and countries, which take into account the rapidly changing costs of petroleum - derived energy resources, environmental damage and limited reserves, have concentrated their efforts on electric car technologies. Electric cars are vehicles that use electrical energy in their drive system.

In the design of road vehicles, forces affecting energy consumption, road holding and acceleration must be considered. The vehicle will only achieve the desired effect when it is designed by calculating the rolling resistance, aerodynamic resistance and climbing resistance forces (Kost, 2014). These forces are the main forces acting on the vehicle and there are many other parameters effective in vehicle design.

The relative motion between air and solid bodies causes some forces on the objects. These forces are examined with the laws of aerodynamics. The design of objects such as aircraft, road vehicles and wind turbines are carried out by analyzing the effect of these forces on the body.

Aerodynamic forces, especially at certain speed values, consumes a significant portion of the power produced by the engine. Therefore, aerodynamic forces and parameters such as vehicle geometry, velocity and weather conditions are effective on these forces have been the subject of many studies as theoretical, numerical and experimental (Windsor, 2014).

1.2 Literature

1.2.1 Literature Search on Aerodynamics of Road Vehicles

Aerodynamic forces acting on the vehicle have been the subject of studies from past to present. These studies have been carried out to create the ideal aerodynamic structure of vehicle body. Geometry of the bodies is effected their drag coefficient as shown in the Figure 1.1.

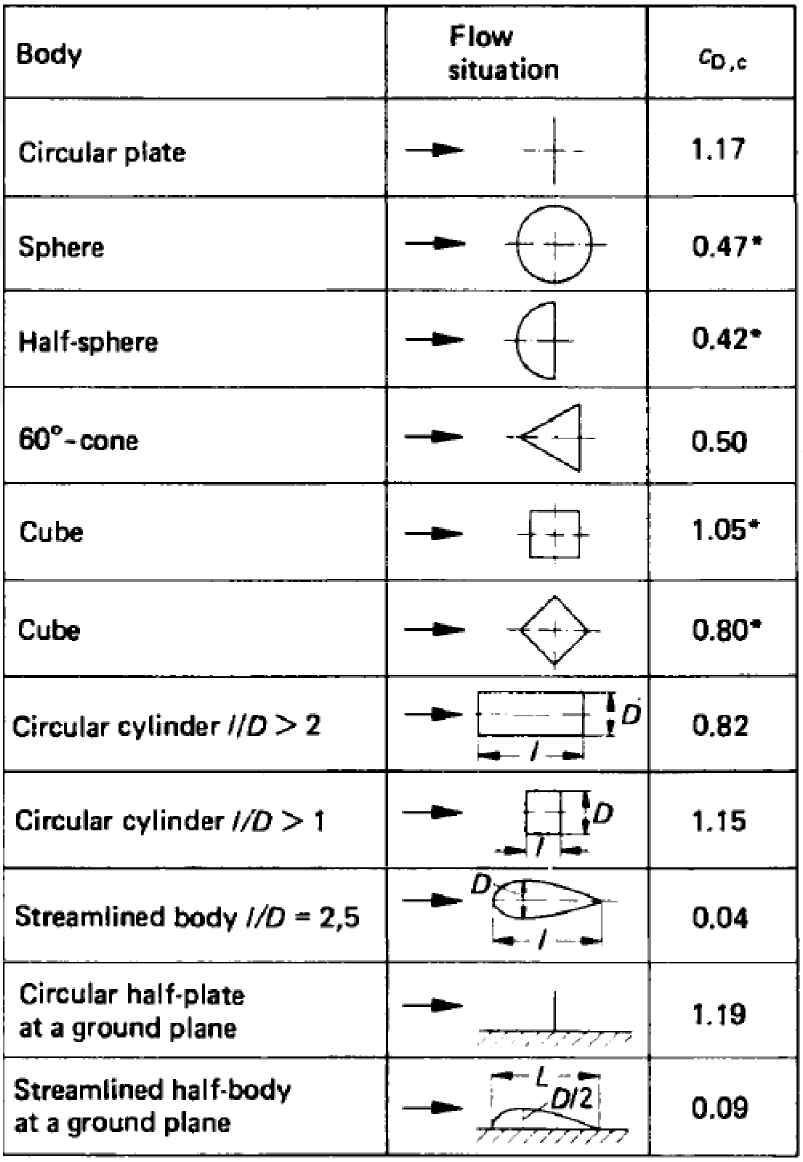

Body	Flow situation	$c_{D,c}$
Circular plate		1.17
Sphere		0.47*
Half-sphere		0.42*
60°-cone		0.50
Cube		1.05*
Cube		0.80*
Circular cylinder $l/D > 2$		0.82
Circular cylinder $l/D > 1$		1.15
Streamlined body $l/D = 2{,}5$		0.04
Circular half-plate at a ground plane		1.19
Streamlined half-body at a ground plane		0.09

Figure 1.1 Different body shapes and their drag coefficient (Hucho, 1986)

The geometric optimizations for reducing the aerodynamic forces acting on the vehicle resulted in a significant reduction of the resistance coefficients (Hucho, 1986).

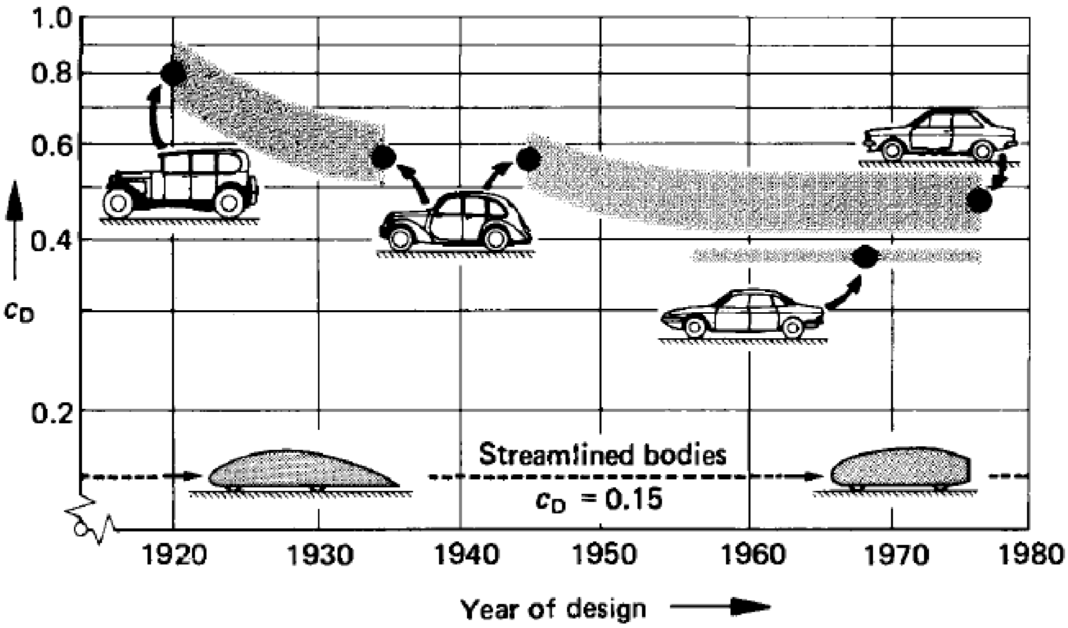

Figure 1.2. Aerodynamic drag reduction, from 1920 to 1970 (Hucho, Janssen & Emmelman, 1976)

Buchheim, Deutenbach & Lückoff (1981) introduced the effective parameters on the aerodynamic drag coefficient. They proposed innovations for passenger cars to be designed and commented the effects of these innovations on the drag coefficient.

Ahmed & Ramm (1984) designed a model (Ahmed model) that facilitates the examination of the effects of the geometric parameters of the vehicle on the flow region. In the following years, various numerical and experimental studies were carried out by using this simplified geometry. Sims-Williams & Dominy (1998) conducted Hot Wire Anemometry (HWA) experiments to examine the unsteadiness and instability of the two different Ahmed body.

Guilmineau (2007) studied numerically with Ahmed models which designed with different slant angles. The flow structure around the bodies were investigated with several turbulence models and compared with experimental results in Lienhart & Becker (2003). Lienhart & Becker (2003) conducted Laser Doppler Anemometry (LDA) and HWA experiments in low speed wind tunnel. Different geometries designed with two different slant angles were investigated and topologies obtain from the flow domain were compared.

Spohn & Gillieron (2002) conducted water tunnel experiments for the Ahmed body to investigate flow separation and swirl structures. In these experiments, they visualized the flow using video acquisition equipment. Although they worked with low Reynolds numbers, they showed that the flow structure is in harmony with the literature and that low speed water tunnels can be used in this type of studies.

Suzuki, Tanemoto & Maeda (2003) examined the impact of regional infrastructure on the aerodynamic characteristics of the vehicle. In the wind tunnel experiments, the effects of the structure of the bridge beam and the wind angle were examined. As a result of this study, it was observed that parameters such as different structures of bridge beam and wind angles change the aerodynamic characteristics by directly affecting the boundary layers on the vehicle.

Watkins & Vino (2008) conducted wind tunnel experiments to examine the effect of vehicle spacing on vehicle aerodynamics. They observed the reduction effect on the lift and drag forces of the vehicle for close spacing.

Nayeri et al. (2014) studied the effect of variable yaw angles on the aerodynamic characteristics of the vehicle with two different rear end geometries (sedan, notchback). Two different geometries demonstrated different flow characteristics in the zero - yaw angle condition. Flow visualizations showed that the increased yaw angle causes a separation bubble from rear window to leeward.

1.2.2 Literature Search on Particle Image Velocimetry (PIV)

Years before the start of PIV studies, Leonardo Da Vinci (lived between 1452 – 1519) was interested in drawing various flow structures and created detailed drawings of water flow patterns as shown in the Figure 1.3. Also, his drawings about human body and flow pattern around aortic valves are still examined and compared with actual studies.

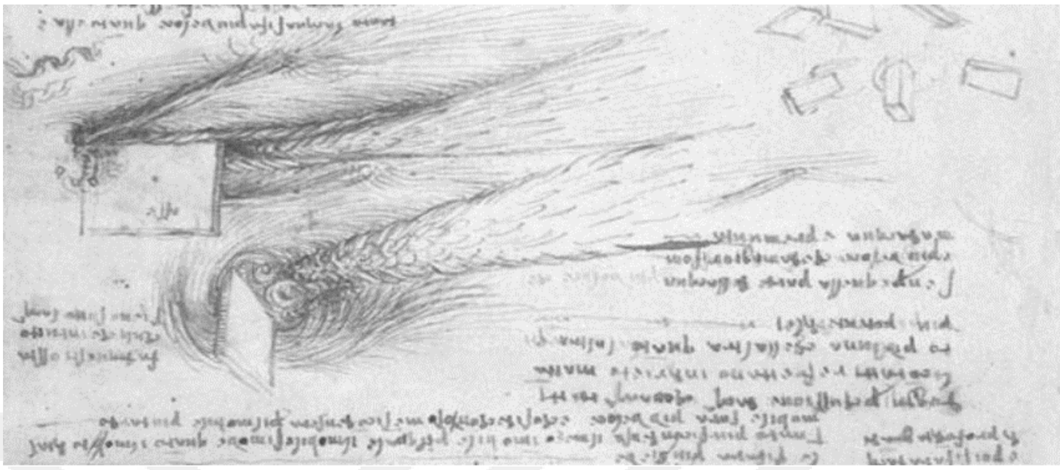

Figure 1.3 Da Vinci’s sketch of turbulence behind obstacle (Basic, 2016)

In the twentieth century, Ludwig Prandtl observed the flow structure in a canal (in the Figure 1.4) where he added particles in water (Raffel, Willert, Wereley & Kompenhans, 2007). By using this experimental setup, he obtained just visual data not quantitative as demonstrated in the Figure 1.5.

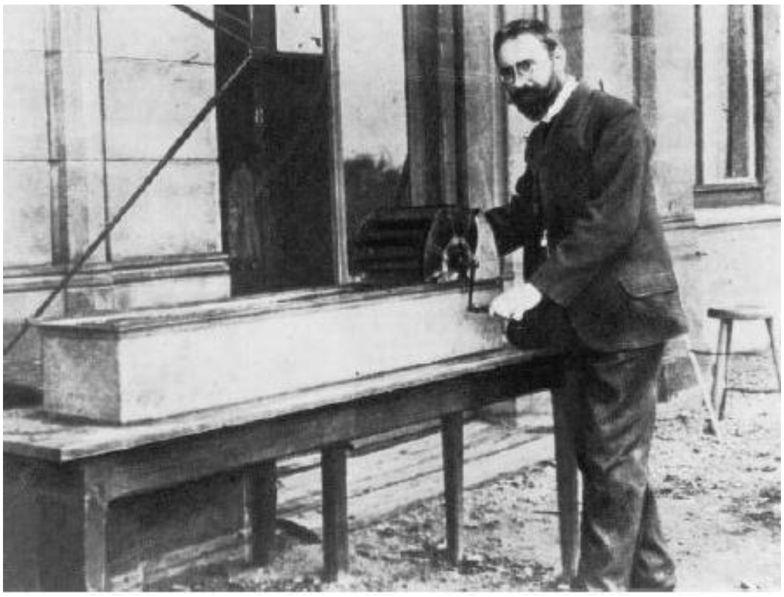

Figure 1.4 Ludwig Prandtl and his experimental setup (Raffel, Willert, Wereley & Kompenhans, 2007).

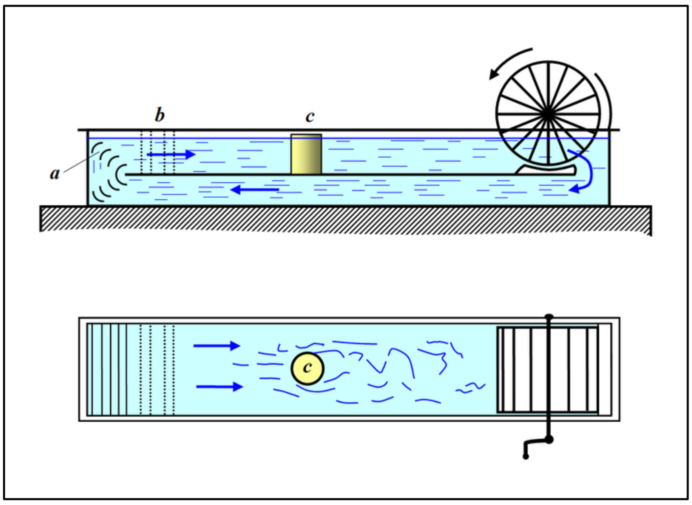

Figure 1.5 Schematic of the experimental setup created by Prandtl (Mars, 2013)

The PIV method, mentioned for the first time in 1984, is a flow visualization with non - intrusive and whole field measurement (Raffel, Willert, Wereley & Kompenhans, 2007; Adrian, 2005).

Depardon et al. (2005) used the near-wall PIV method to obtain the skin friction topology on planar surfaces. In addition to their PIV experiments, they compared the results obtained by performing oil-flow visualization as shown in the Figure 1.6. They obtained close pattern when Reynolds number values is equal to 160,000.

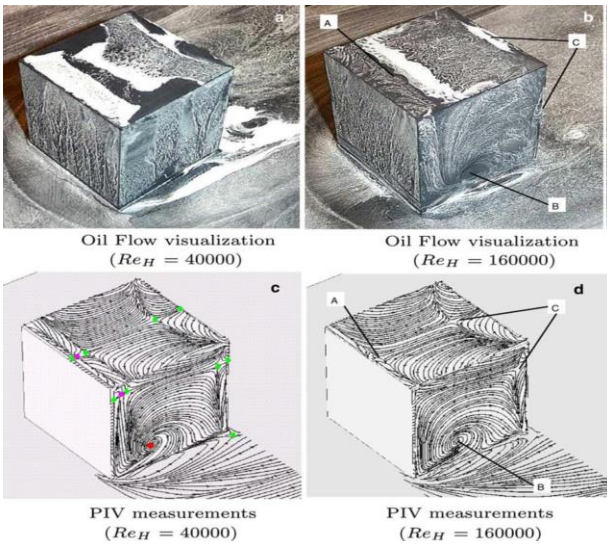

Figure 1.6 Cube geometry topology (Depardon et al., 2005)

Depardon, Lasserre, Brizzi & Boree (2006) conducted near-wall PIV experiments for simplified vehicles designed by using different slant angles and sized 1/4 scale. They obtained time-averaged wake flow patterns for each rear-end geometry. As a result of this study, square back pattern was obtained for 10° and 41°, while fastback pattern was obtained for 30°.

Kim et al. (2006) examined the flow and vortex structure around spoiler of road vehicle with PIV experiments. The vehicle was scaled by 1/43 and the experiments were carried out in the water tunnel. The flow around vehicle demonstrated a wide difference for vortex structure with the presence of spoilers.

McCutcheon, McColgan, Grant & Hurst (2002) conducted PIV experiments at 20 m/s free stream velocity over Ahmed models designed at different rear end angles, which were scaled by 1/8. As a result of the study, the velocity distribution and the vorticity of the flow area were obtained. These distributions are important in determining the aerodynamic drag and lift coefficients. In addition, this study also emphasized that the vortices in the flow area have developed in various structures.

Gürlek, Sahin & Ozkan (2012) carried out PIV experiments in a water tunnel by using scaled bus geometry. The structure of vorticity around body examined both for time-averaged and instantaneous flow. The differences were observed between these flow structures.

1.2.3 Literature Search on Computational Fluid Dynamics (CFD)

Modi, Hill & Yokomizo (1995) stated that the power produced by an engine at a speed of 100 km/h is used for aerodynamic resistance around 50% to 70%. Considering the effect of these consumption values on energy economy, besides experimental studies aimed at reducing aerodynamic resistances, solution suggestions are presented in numerical domain. Also these numerical studies were used for comparing and validating with experimental data.

Rajsinh & Raj (2012) presented numerical simulation of flow structure around Ahmed body with the slant angle 20° for two different velocity values (40 m/s, 60 m/s). They used ACUSOLVE CFD commercial package program to solve Spallart–Allmaras turbulence model and obtained topology of flow domain around wake region.

Song et al. (2012) proposed an aerodynamic optimization by making changes on the rear body of a sedan. In this study, Artificial Neural Networks (ANN) was used and the drag coefficient was calculated. 64 different cases for rear body is analyzed for optimization and obtained drag coefficient value is equal to 0.251. This C_D value is reduced by 5.639% compared to baseline.

Hetawala, Gophaneb, Ajay & Mukkamalad (2014) conducted CFD analyzes for a race car geometry. In this analysis, he examined the effect of front spoiler and firewall vent. With this study, it was aimed to obtain the minimum drag coefficient. They used the ANSYS Fluent package program and the k - epsilon turbulence model in their analysis. The most effective modification was observed as car body with front wing and firewall of cut section.

Desai, Channniwala & Nagarsheth (2008) carried out numerical and experimental studies for 1/15 scaled model car. Fluent is used for numerical study as a solver. At the end of the study, the comparison between the drag coefficient values obtained from experimental and numerical studies was compared. They also examined the effect of Reynolds number on the coefficient of resistance.

Parab et al. (2014) calculated the drag and lift forces on the model car with the help of Ansys CFX package program. Realizable k-epsilon was chosen as the turbulence model. Diffuser was added to vehicle according to the results they obtained from the initial geometry and compared the results in terms of C_D, C_L and velocity distribution.

Flow separations are one of the most dominant reason for the aerodynamic drag, therefore discontinuance of the streamlines must be observed. Koike, Nagayoshi & Hamamoto (2004) obtained the flow separations on the rear side of the sedan car. The vortex generators were added to the main geometry to decrease drag. The designs with and without vortex generators were investigated in terms of flow separations. Also, when the car is designed by using vortex generators 0.006 reduction in both the drag and lift coefficient.

Ozawa, Nishikawa & Higashida (1998) stated that the aerodynamics characteristics can be represent with multiplication of drag coefficient and frontal projected area (C_D*A). They created alternative designs for solar car and compared these designs in term of their aerodynamic drag by analyzing with Computational Fluid Dynamics (CFD) and wind tunnel experiments.

1.3 Aim and Motivation

The aim of this study is to determine the aerodynamic characteristics of an electric vehicles. In this sense, the parameters that vary according to the flow and flow structure to be formed around the vehicles were examined.

Within the scope of this study, the electric vehicles designed with different front and rear geometry were modeled on a certain scale. These models were prepared for experimental study with three-dimensional printer. Particle Image Velocimetry (PIV) experiments were conducted in the wind tunnel, which prepared for providing the flow domain around the vehicle. In addition, the three dimensional numerical models of the vehicles were created by using commercial software ANSYS Fluent. The velocity and velocity-related characteristics obtained from these models, which were created by using CFD method, were compared with the data obtained from the PIV experiments. The coherence of the experimental and numerical results was evaluated in terms of flow separations, velocity magnitudes and direction. This evaluation provided validation for the next series of numerical analysis with different flow field parameters. The effects of different geometric design parameters on velocity maps and flow separations were investigated and compared. Numerical analysis of different velocities acting on the electric vehicle geometries were carried out and the effect of different parameters on the flow region was compared. Also, the effects of different turbulence models and dimensionless wall distance (mesh structure) on the accuracy were investigated. According to the obtained results, parameters which minimize the aerodynamic forces on the vehicle were determined. Thus, the external flow structure of the vehicle designed in near-real geometry is obtained and verified both numerically and experimentally.

CHAPTER TWO
THEORETICAL STUDY

2.1. Dimensional Analysis

The structure of the experimental setups in the studies is crucial in terms of the time, cost and technical support. In this sense, experiments conducted over a scaled model have been widely used in design processes. The usage of these scaled models only provides valid results under certain conditions. Therefore, the geometric, kinematic and dynamic effects of the model should be taken into account.

The most important parameter considered in terms of similarity conditions in flow problems is the Reynolds number (Re) which is the dimensionless ratio of inertial forces to viscous forces. When the Reynolds numbers of the model and prototype are equal, the similarity of the flow around vehicle geometry can be obtained. In this case, the Reynolds number, calculated for the prototype at the velocity of 26 m/s, can be obtained with the velocity of 416 m/s for the model reduced by 1/16 as illustrated in the Figure 2.1. In these velocities, the incompressible flow approach should be discussed. In addition, dimension analysis and control over the Mach number is required. The velocity value for the model (V_M) is calculated as shown in Equation 2.1.

$$V_M = V_P \left(\frac{\mu_M}{\mu_P}\right)\left(\frac{\rho_P}{\rho_M}\right)\left(\frac{L_P}{L_M}\right) \tag{2.1}$$

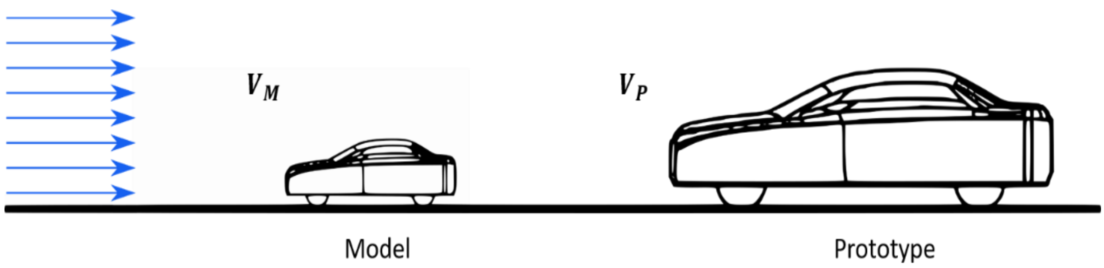

Figure 2.1 Schematic illustration of the geometric similarity

The aerodynamic drag coefficient (C_D) is unclear in the low Reynolds numbers for the vehicles in a flow area. The drag coefficient is a dimensionless aerodynamic characteristic of a vehicle. As the Reynolds number increases, the effect on the drag coefficient can be neglected. From the point of this increment where the resistance coefficient does not change, the Reynolds independency is obtained (Cengel & Cimbala, 2006).

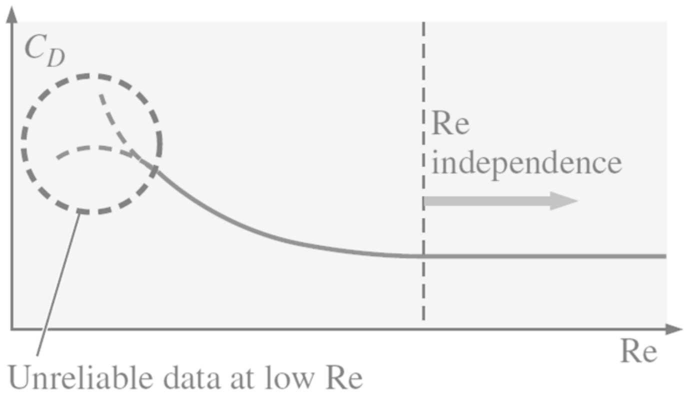

Figure 2.2 Reynolds number independency (Cengel & Cimbala, 2006)

2.2 Aerodynamics of Road Vehicles

2.2.1 Drag and Lift Force

Drag and lift forces are formed on the body which moves relative to the air. These forces are the components of the pressure and shear forces on the body. Three main forces is occurred on the car body; resistance force against to the impulse of the motor, lift force perpendicular to the ground plane and side force due to wind angle (Hucho, 1986). These forces were illustrated as Figure 2.3.

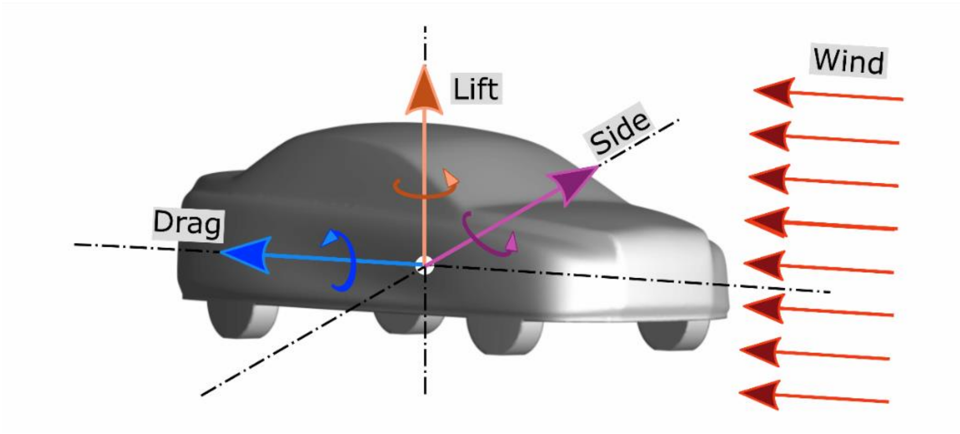

Figure 2.3 Aerodynamic forces acting on the car

The geometric structure of the object is expressed with the dimensionless parameters, called resistance and lift coefficient, represents a significant advantage in comparing the aerodynamic characteristics of the bodies. Drag and lift coefficients are obtained as below (Equation 2.2 and Equation 2.3). In these equation projected area on the flow direction is represented with *A* (is shown in the Figure 2.4), F_D and F_L are drag and lift force respectively, *V* is used for free stream velocity of air, ρ is density of air.

$$C_D = \frac{F_D}{0.5\rho V^2 A} \tag{2.2}$$

$$C_L = \frac{F_L}{0.5\rho V^2 A} \tag{2.3}$$

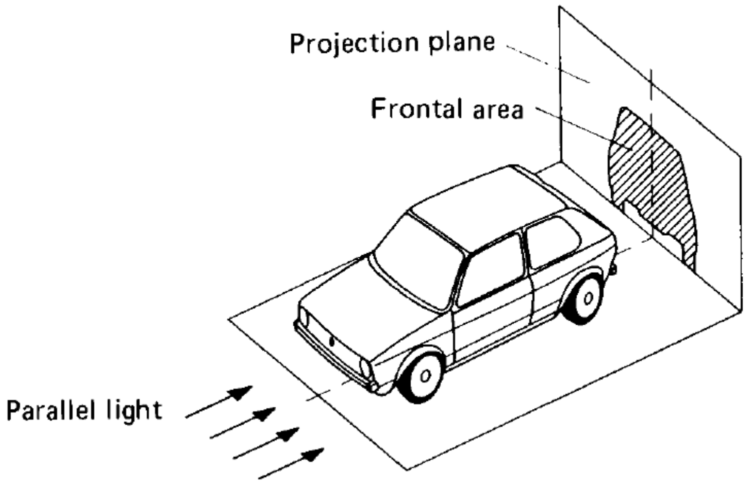

Figure 2.4 Demonstration of projected frontal area (Hucho, 1986)

2.2.2 Streamlined Body and Flow Separations

The fluid moving at a sufficient velocity in a flat flow area separates itself instead of adhering to the curves of the surface when it encounters a curvilinear geometry. The sharpness of the object, the surface roughness, achieved Reynolds number and the vorticity are effective parameters on these separations. As a result, a low pressure zone is formed by separating from the streamlines (Cengel & Cimbala, 2006). The structure of the flow separations, the region where it occurs and the pressure of the separated area are important factors to be considered in the design processes. Different flow separations configurations for various angle of rear end are demonstrated in the Figure 2.5. In addition, the effect of rear end geometry on the drag coefficient is as shown in Figure 2.6.

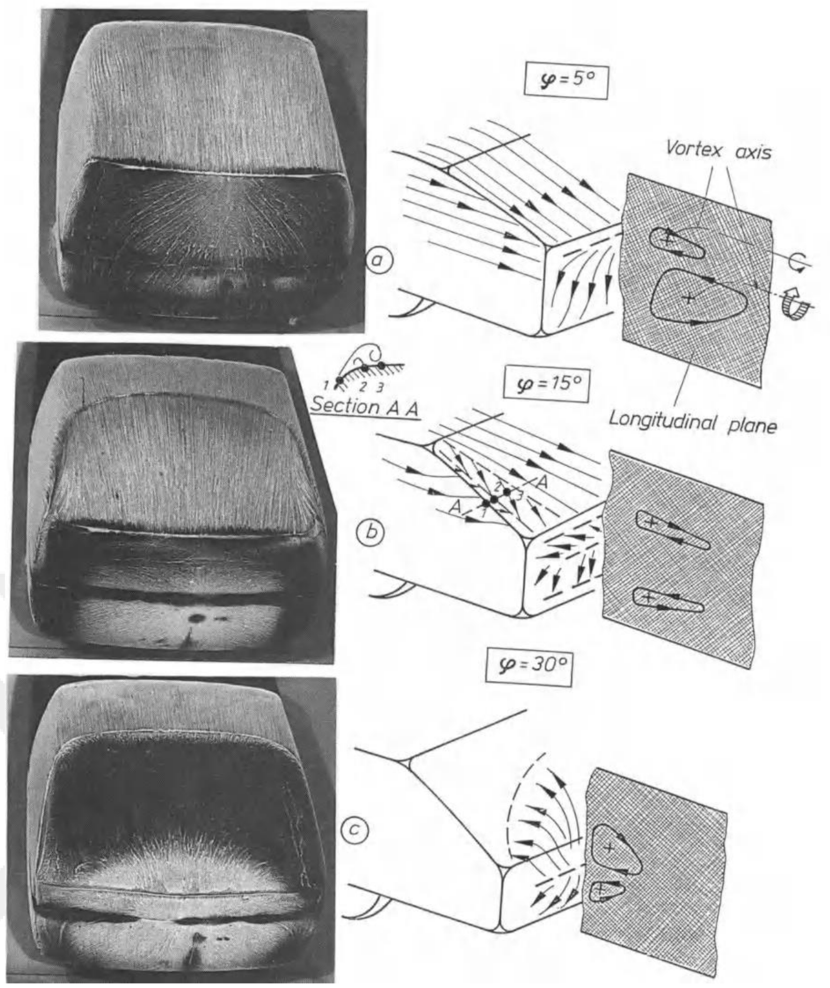

Figure 2.5 Flow separation structures for different rear end geometries (Hucho, 1986).

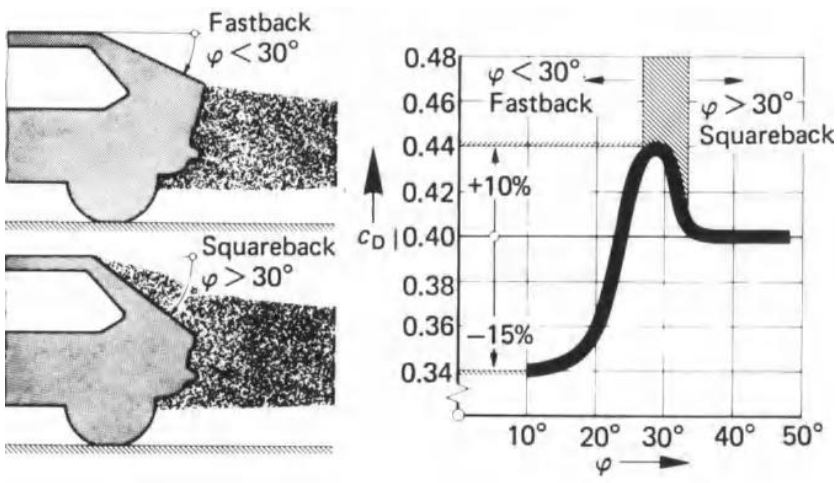

Figure 2.6 Drag coefficient values for different rear end (Hucho, 1986).

Streamlined and bluff bodies are used widely to characterize flow separations and forces on the geometry. The main reason of drag force for streamlined body is shear stress. Besides, for the bluff body, the drag is generated from the pressure forces with a very large proportion. Various bluff bodies and streamlined (aerodynamic) body are illustrated as in Figure 2.7.

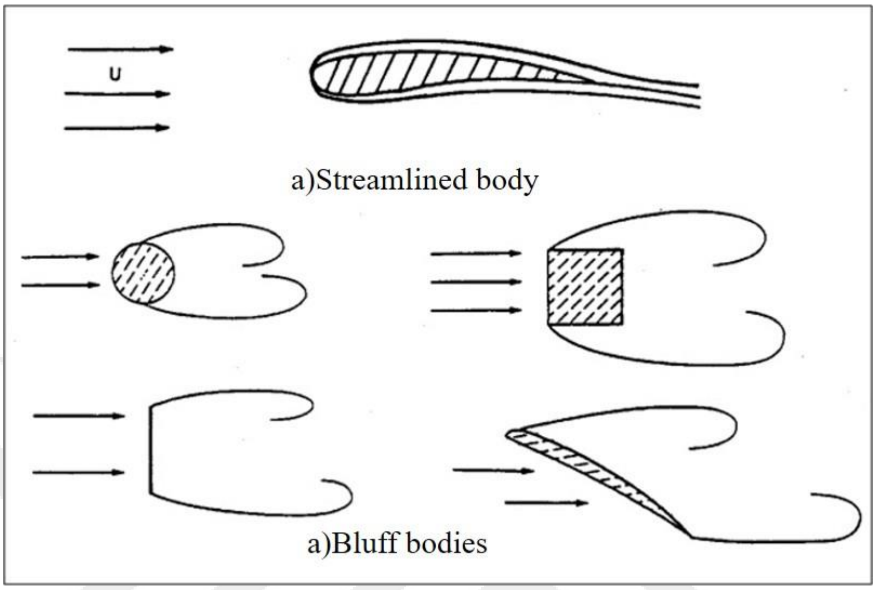

Figure 2.7 Different body shapes (Buresti, 2000)

CHAPTER THREE
NUMERICAL STUDY

The experimental investigation for each parameter of a fluid domain problems is limited in terms of time, cost and labor. In this sense, flow problems have been solved by using Computational Fluid Dynamics (CFD) method and compared with experimental studies for accuracy rate. CFD studies are mostly done by dissolving the governing equations within the computer domain by using certain assumptions. Therefore, the commercial package programs such as ANSYS Fluent, ANSYS CFX and STAR-CCM+ are preferred for the solution of these problems. In this study ANSYS Fluent was used to solve aerodynamic state of scaled vehicle bodies. Specific steps and theoretical background are required to create a computational environment for flow-domain. Three basic steps are determined for the analysis as follows,

- Pre-processing (Geometry, Mesh)
- Physical setup (Boundary and initial conditions, models and so on)
- Post-processing (Compute the solutions, examine results and so on)

After the analysis steps, literature studies or experimental studies should be used to validate and compare the results.

3.1 Theory of the Computational Fluid Dynamics

Computational fluid dynamics problems are solved by three basic governing equations.

- Continuity equation (Mass conservation principle)
- Momentum equation (Newton’s second law)
- Energy equation (Not activated in this study)

In cases where the flow is turbulent, the Reynolds-Averaged Navier Stokes (RANS) equation is used instead of Navier-Stokes equation (Cengel & Cimbala, 2006; Ansys Fluent User Guide, 2012). In this sense, turbulence models in which RANS equations are solved can be used to calculate the Reynolds stresses. The RANS - based turbulence models in use are as shown in the Figure 3.1.

The chosen turbulence model requires the calculation of new equations in addition to the equations mentioned above. For example, the standard k-epsilon model is solved with two transport equations besides the basic equation set.

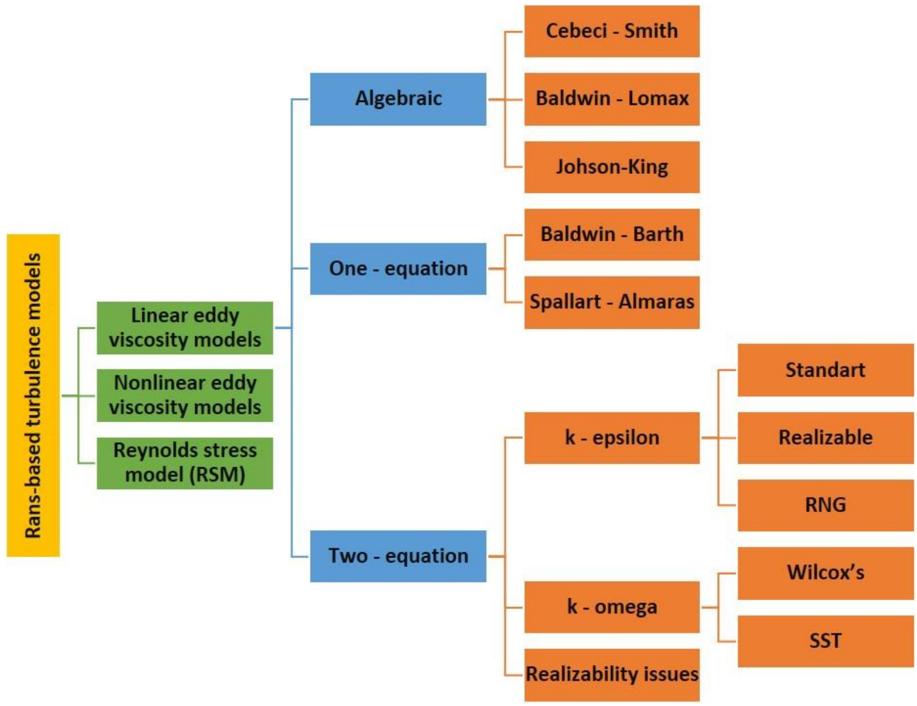

Figure 3.1 Turbulence models for CFD

3.1.1 Governing Equations for Numerical Study

In this study the continuity and momentum equations are used as given below. In these equations, u is x - velocity, v is y - velocity and w is z – velocity. Also, terms with B represent body forces, τ is used for shear stress.

Continuity:

$$\frac{\partial u}{\partial x}+\frac{\partial v}{\partial y}+\frac{\partial w}{\partial z}=0 \tag{3.1}$$

Momentum:

$$u\frac{\partial u}{\partial x} + v\frac{\partial u}{\partial y} + w\frac{\partial u}{\partial z} = -\frac{1}{\rho}\frac{\partial p}{\partial x} + \frac{1}{\rho}\left(\frac{\partial \tau_{xy}}{\partial y} + \frac{\partial \tau_{xz}}{\partial z}\right) + B_x \quad (3.2)$$

$$u\frac{\partial v}{\partial x} + v\frac{\partial v}{\partial y} + w\frac{\partial v}{\partial z} = -\frac{1}{\rho}\frac{\partial p}{\partial y} + \frac{1}{\rho}\left(\frac{\partial \tau_{xy}}{\partial x} + \frac{\partial \tau_{yz}}{\partial z}\right) + B_y \quad (3.3)$$

$$u\frac{\partial w}{\partial x} + v\frac{\partial w}{\partial y} + w\frac{\partial w}{\partial z} = -\frac{1}{\rho}\frac{\partial p}{\partial z} + \frac{1}{\rho}\left(\frac{\partial \tau_{xz}}{\partial x} + \frac{\partial \tau_{yz}}{\partial y}\right) + B_z \quad (3.4)$$

3.1.2 Realizable k-ε turbulence model

Standard k–ε model includes two transport equations, which are used to determine turbulence. Transport equations are solved for turbulent kinetic energy (k) as given with Equation 3.5 and turbulent dissipation (ε) can be calculated as shown with Equation 3.6 (ANSYS Fluent User Guide, 2012).

Transport equation for k;

$$\frac{\partial}{\partial t}(\rho k) + \frac{\partial}{\partial x_i}(\rho k u_i) = \frac{\partial}{\partial x_j}\left[\left(\mu + \frac{\mu_t}{\sigma_k}\right)\frac{\partial k}{\partial x_j}\right] + P_k + P_b - \rho\varepsilon - Y_M + S_k \quad (3.5)$$

Transport equation for ε;

$$\frac{\partial}{\partial t}(\rho\varepsilon) + \frac{\partial}{\partial x_i}(\rho\varepsilon u_i) = \frac{\partial}{\partial x_j}\left[\left(\mu + \frac{\mu_t}{\sigma_\varepsilon}\right)\frac{\partial \varepsilon}{\partial x_j}\right] + C_{1\varepsilon}\frac{\varepsilon}{k}(P_k + C_{3\varepsilon}P_b) - C_{2\varepsilon}\rho\frac{\varepsilon^2}{k} + S_\varepsilon \quad (3.6)$$

With the constants given in Table 3.1,

Table 3.1 Values of constants given in transport equation

CONSTANT	VALUE
$C_{1\varepsilon}$	1.44
$C_{2\varepsilon}$	1.92
σ_k	1.0
σ_ε	1.3
C_μ	0.09

Turbulent viscosity is represented with μ_t and obtained by using Equation 3.7. C_μ is variable for Realizable k-ε turbulence model. The realizable k-epsilon turbulence model is more effective for the flows which included in separations.

$$\mu_t = \rho C_\mu \frac{k^2}{\varepsilon} \tag{3.7}$$

In these equations, $P_{k,}$ refers to the part of the turbulence kinetic energy that results from the average velocity gradient and can be calculated with Equation 3.8. S is the modulus of the mean rate of strain tensor and can be obtained by using Equation 3.9. The dilatation dissipation, Y_M, can be obtained with Equation 3.13.

$$P_k = \mu_t S^2 \tag{3.8}$$

$$S \equiv \sqrt{2S_{ij}S_{ij}} \tag{3.9}$$

$$S_{ij} = \frac{1}{2}\left(\frac{\partial u_i}{\partial u_j} + \frac{\partial u_j}{\partial u_i}\right) \tag{3.10}$$

Effect of buoyancy is calculated with Equation 3.11. In this equation β is thermal expansion coefficient and determined by using Equation 3.12.

$$P_b = \beta g_i \frac{\mu_t}{Pr_t}\frac{\partial T}{\partial x_i} \tag{3.11}$$

$$\beta = -\frac{1}{\rho}\left(\frac{\partial \rho}{\partial T}\right)_p \tag{3.12}$$

$$Y_M = 2\rho\varepsilon M_t^2 \tag{3.13}$$

$$M_t = \sqrt{\frac{k}{a^2}} \tag{3.14}$$

3.1.3 Shear Stress Transport (SST) k-ω turbulence model

Standard k – ω model includes two transport equations, which are used to determine turbulent properties. These equations are solved for kinetic energy (k) and turbulent frequency (ω).

Transport equation for k:

$$\frac{\partial k}{\partial t} + U_J \frac{\partial k}{\partial x_j} = \tau_{ij}\frac{\partial U_i}{\partial x_j} - \beta^* k\omega + \frac{\partial}{\partial x_j}\left[(\nu + \sigma^* \nu_T)\frac{\partial k}{\partial x_j}\right] \tag{3.15}$$

Transport equation for ω;

$$\frac{\partial \omega}{\partial t} + U_J \frac{\partial \omega}{\partial x_j} = \alpha\frac{\omega}{k}\tau_{ij}\frac{\partial U_i}{\partial x_j} - \beta\omega^2 + \frac{\partial}{\partial x_j}\left[(\nu + \sigma\nu_T)\frac{\partial \omega}{\partial x_j}\right] \tag{3.16}$$

Kinematic Eddy viscosity is represented with ν_T and can be calculated from Equation 3.17.

$$\nu_T = \frac{k}{\omega} \tag{3.17}$$

With these constants given in Table 3.2,

Table 3.2 Values of constants given in transport equation for ω

CONSTANT	VALUE
$\boldsymbol{\alpha}$	5/9
$\boldsymbol{\beta}$	3/40
$\boldsymbol{\beta}^*$	9/100
$\boldsymbol{\sigma}$ **and** $\boldsymbol{\sigma}^*$	1/2

SST k- ω turbulence model is more useful than the standard k- ω for the flow regions where the adverse pressure gradient observed.

3.2 Steps for CFD

3.2.1 Pre-processing

3.2.1.1 Preparing Vehicle Geometry

Vehicle geometries contains compelling components for the complex solution structure of computational fluid dynamics. In this sense, a simple structures were obtained by ignoring the mirrors, hood and door gaps on the actual models. In addition, planes for both vehicles (dimensions can be neglected) were created from the point where the vehicles meets the ground plane to obtain better mesh quality and avoid higher skewness and linear contact.

Geometries were modeled by using a commercial CAD software SolidWorks 2017, taking into account the above mentioned simplification studies. Due to the curved surfaces of the vehicles, it is difficult to directly model solid body as three dimensionally. Therefore, shell geometries were created using surface tools as a closed volume. The enclosed volume formed by the surfaces was converted into solid model and the vehicle geometries were modeled on 1/24 scale. The views of the vehicle geometries are as shown in Figure 3.2.

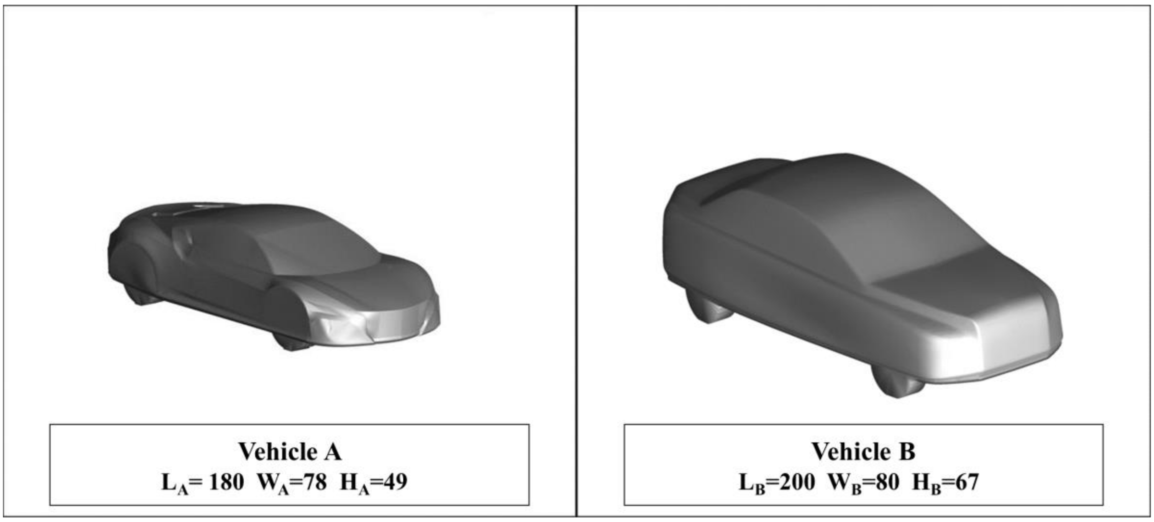

Figure 3.2 Schematic illustration of Vehicle A and Vehicle B (Dimensions were given in mm – both scaled by 1/24)

The vehicle geometries contained two sub-geometries as lower and upper parts as demonstrated in Figure 3.3. The geometry of the vehicle to be used in the experimental study that will be described in the following chapters was designed as two different body to easily obtain 3D Printing.

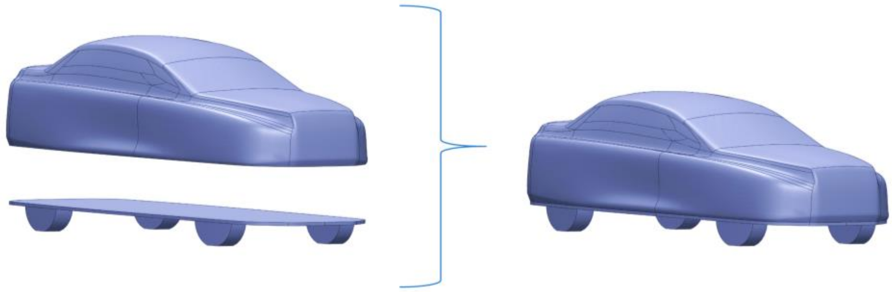

Figure 3.3 Car body and its sub-geometries

3.2.1.2 Preparing Fluid Domain

The fluid domain surrounding the vehicle geometry to be studied experimentally in the wind tunnel was modelled to be coherent with experimental conditions. In order to simplify the solution in the computational domain, the flow area was half-modelled by considering the vehicle symmetry. The cross section layout of flow region and symmetry plane are shown in the Figure 3.4.

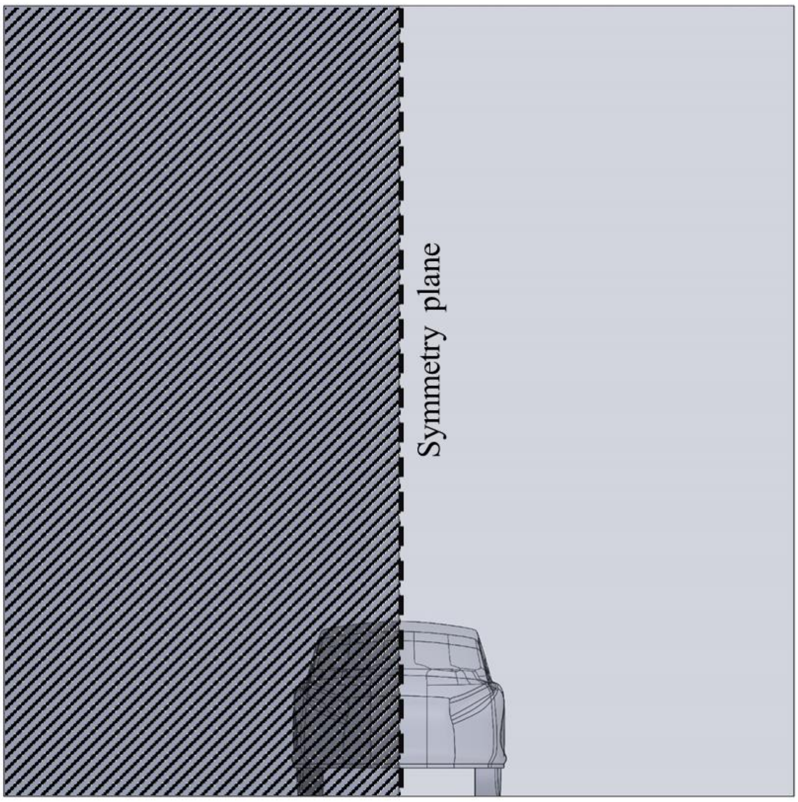

Figure 3.4 Symmetry axis of fluid domain and vehicle body

The vehicle geometries, which were located within the square cross sectional flow area, were subtracted from the external flow area to obtain the computational domain. The geometric dimensions of the computational domain were characterized by the length, which measured from flow direction on the vehicle. *L* was represented the length of car and is equal to 200 mm (for Vehicle B). Other dimensions were determined with this length as shown in the Figure 3.5. The same dimensions were chosen for the Vehicle A.

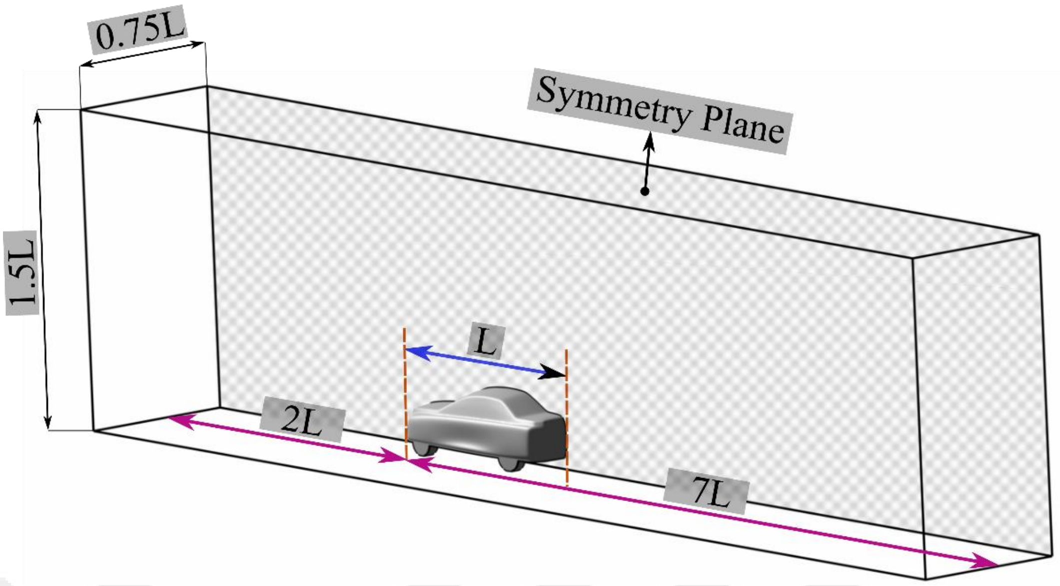

Figure 3.5 Computational fluid domain with characterized dimensions

3.2.1.3 Mesh Structure

The obtained flow domain must be discretized into finite elements to solve conservation and transport equations. These elements can be generated by 3 different methods as below and Fluent uses Finite Volume Method which is special form of Finite Difference Method.

- Finite Difference Method
- Finite Elements Method
- Spectral Methods

In this study, the flow domains were divided into the calculation regions using ANSYS Meshing. The special conditions created by the different turbulence models require different mesh structures to be used for these models. Two different mesh structures were generated by considering these special conditions. The generated mesh structures are similar in number of elements. However, the first layer thickness and number of layers of the elements formed from the vehicle geometry are different. This difference can be explained by y^+, which is a dimensionless parameter. Detailed explanations on y^+ were described in Section 3.2.1.5.

The flow domains were divided into finite volumes to prepare for numerical solution by using ANSYS Meshing. The mesh structures for each vehicle were created based on the y^+ value required by the turbulence model used. In this context, the effect of the mesh structures on the sensitivity of the velocity boundary layer was investigated.

A dimensionless parameter, y^+, is used to calculate the thickness of the first layer that interacts with the solid body. Realizable k-ε with standard wall function and SST k-ω were used as turbulence models in this study. The y^+ value for the realizable k-ε turbulence model ranges from 30 to 300. For the SST k-ω turbulence model, this value should be approximately 1. The mesh structure used in realizable k-ε turbulence model was created as shown in the Figure 3.6.a and 3.7.a ($y^+ \cong 35$). First layer thickness was calculated according to turbulence model. The mesh structure for the SST k-w turbulence model ($y^+ \cong 1$) was formed with thinner (compared the mesh for Realizable k-ε) first layer thickness and was as shown in Figure 3.6.b and 3.7.b. This structure was created in the same way for the other vehicle (y^+, first layer thickness and number of the layers).

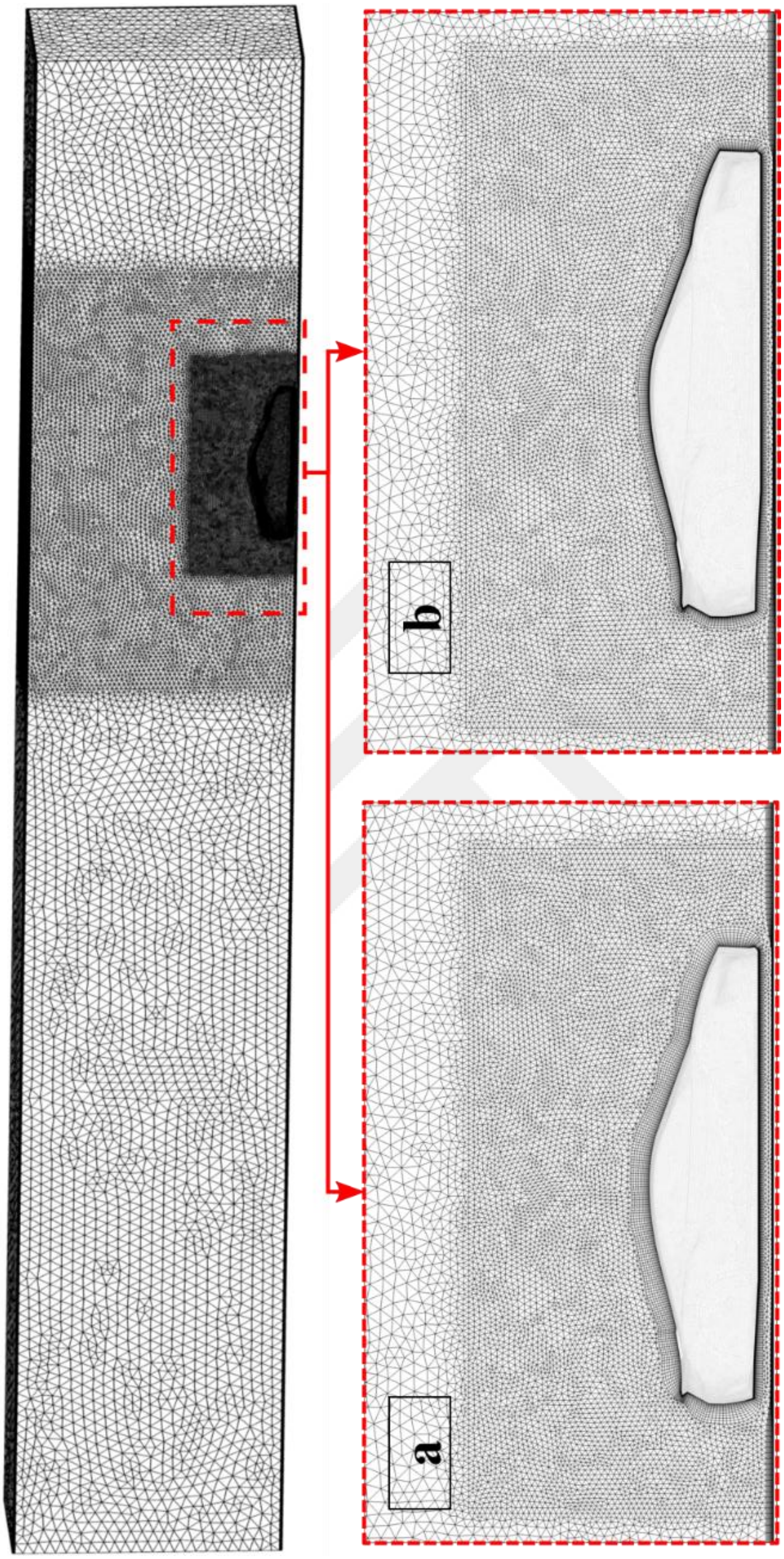

Figure 3.6 Mesh structures of Vehicle A, a. Mesh structure for realizable k-ε turbulence model ($y^+ \cong 35$) b. Mesh structure for SST k-ω turbulence model ($y^+ \cong 1$)

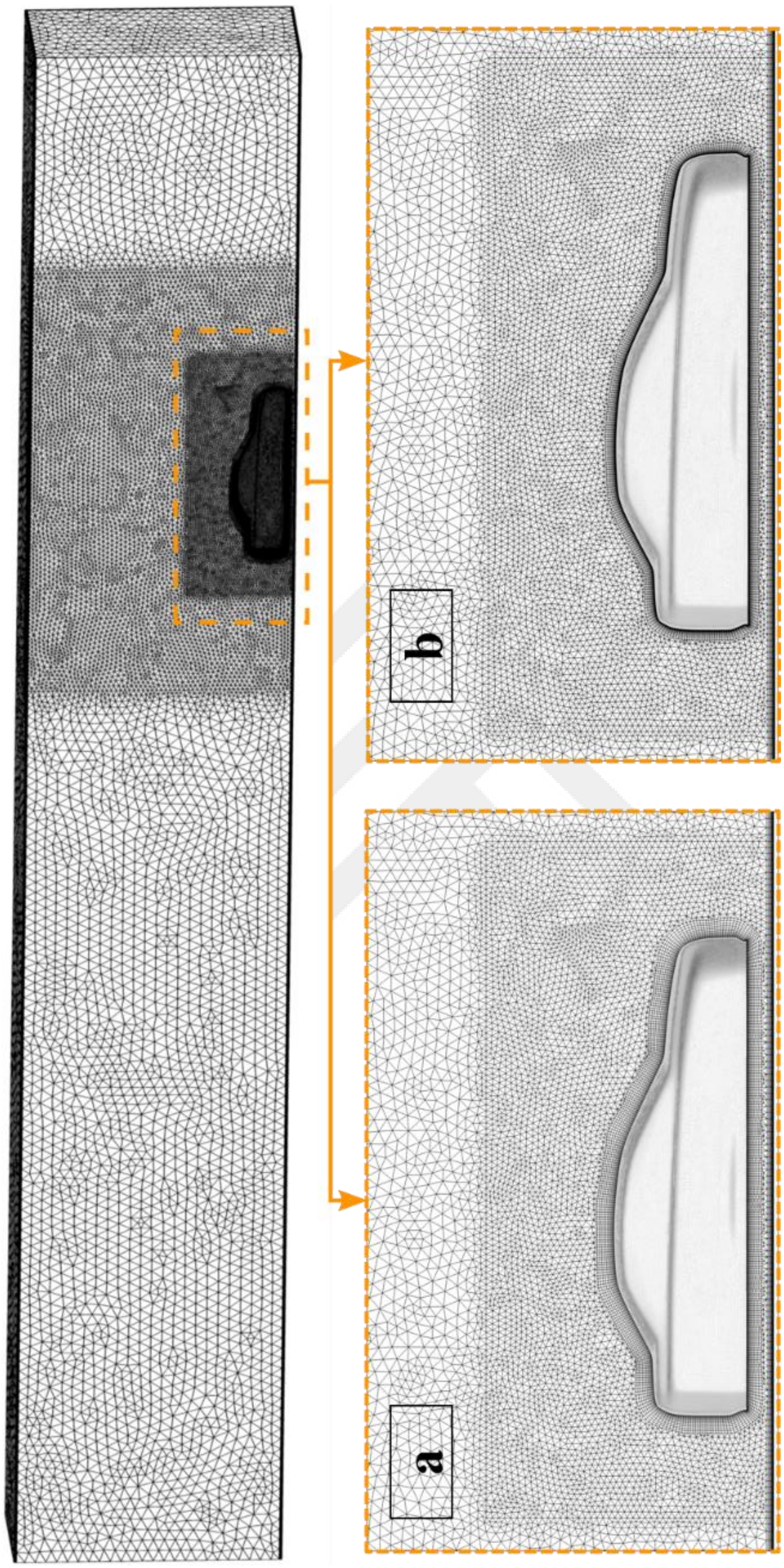

Figure 3.7 Mesh structures of Vehicle B, a. Mesh structure for realizable k- ε turbulence model ($y^{+}\cong$ 35) b. Mesh structure for SST k-ω turbulence model ($y^{+}\cong 1$)

3.2.1.4 Mesh Independency

Mesh quality, orthogonality and skewness values have a great effect on the accuracy of numerical studies. For this reason, these criteria should be taken into consideration when determining the number and type of mesh. In addition, the effect of the selected turbulence model on the mesh structure is described in the next section. The mesh structure created by considering all these conditions should be evaluated by the mesh independency. Mesh independency is obtained for the numerical model when the effect of increasing cell number on the result is lost.

In this study, 5 different mesh numbers were analyzed to examine the effect of increasing mesh number on drag and lift coefficients. The results obtained from different cell numbers are as shown in the Figure 3.8. Approximately mesh number was chosen as 1600000, because of the drag and lift coefficients were found with 0.2% error after these cell number.

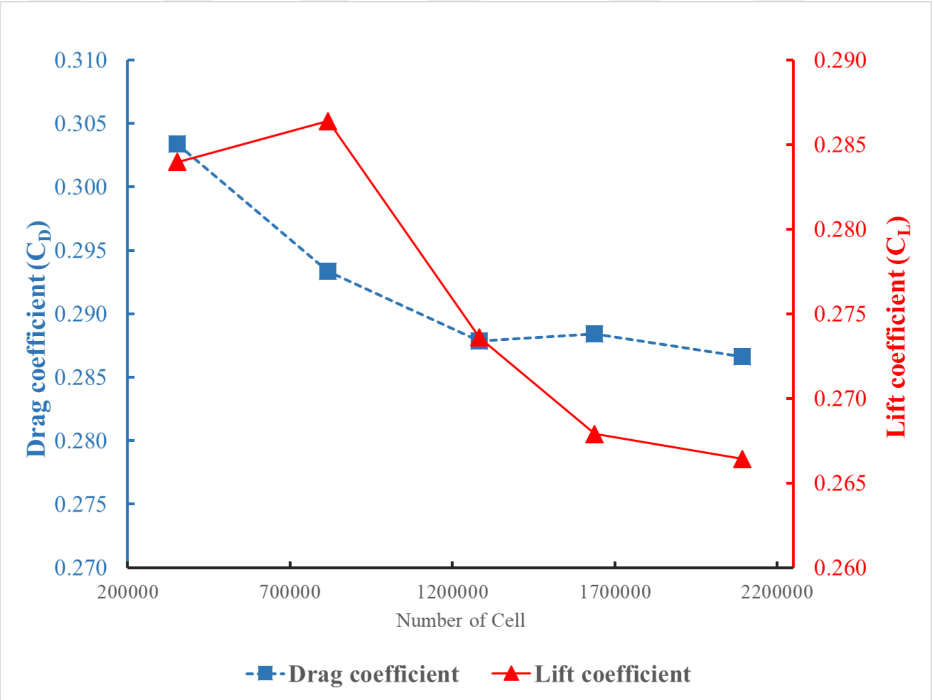

Figure 3.8 The effect of cell number on the drag and lift coefficient

3.2.1.5 Estimation and Effect of Y Plus (Y^+) Value

In order to obtain accurate results from turbulence models, it is important to determine the first layer thickness by selecting the y^+ values according to the model. The velocity profile, which develops almost linearly for laminar flow conditions, is not valid for turbulent flow. Therefore, a detailed examination of the flow near the wall is required. In this sense, the mesh structure to be used in these regions to provide the requirements of the turbulence models, increases the accuracy of the analysis.

The effect of two different mesh structures in the accuracy of the velocity profile in domain near the wall was compared in the Figure 3.9. Figure 3.9.a demonstrates coarse structure through the wall in the y-direction. In addition, the fine mesh structure was demonstrated with Figure 3.9.b. Thus, for the capture of the logarithmic velocity profile, the mesh structure given in Figure 3.9.b is more suitable.

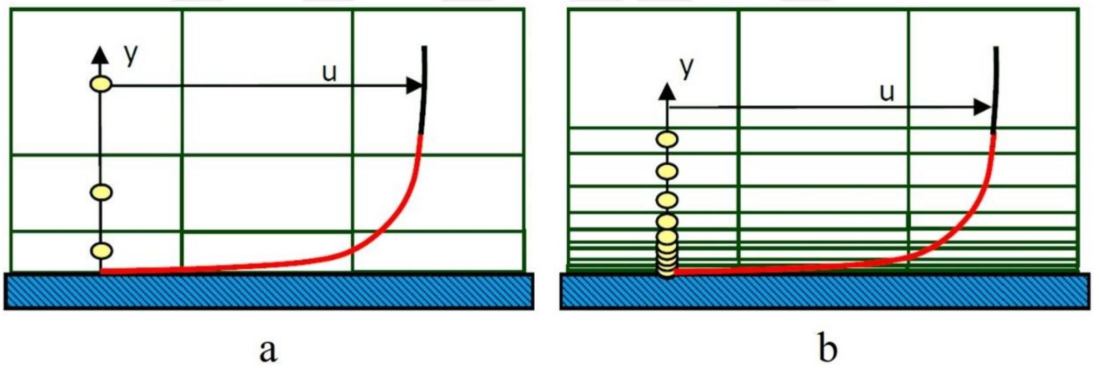

Figure 3.9 a. coarse mesh structure b. fine mesh structure through wall (ANSYS Fluent User Guide, 2012)

The calculation of the first layer thickness, which is suitable for the desired y^+, is given by Equation 3.18.

$$y = \frac{y^+ \mu}{U_T \rho} \tag{3.18}$$

Where y^+ is the dimensionless value, which desired for different turbulence models and flow conditions. ρ is density and μ dynamic viscosity of the fluid. U_T is frictional velocity and can be calculated by using Equation 3.19.

$$U_T = \sqrt{\frac{\tau_w}{\rho}} \tag{3.19}$$

τ_w is wall shear stress and is calculated with Equation 3.20.

$$\tau_w = \frac{1}{2}\rho C_f U^2 \tag{3.20}$$

Where U is freestream velocity and C_f is skin friction coefficient. C_f is obtained by using Equation 3.21 for external flows.

$$C_f = 0.058Re^{-0.2} \tag{3.21}$$

For different turbulence models used in this study, y^+ values determined in literature are as follows. For k-ε turbulence model with standard wall functions, it was recommended to select between 30 and 300. This value was determined as approximately 35 and the first wall height was calculated. For k- ω should be about 1. The first layer thickness calculated for this value was applied to the mesh structure.

The details of two different mesh structures were shown in the Figure 3.6 and Figure 3.7. The mesh structures shown in Figure 3.6.a and 3.7.a are for the case where the y^+ value is equal to 35. Figure 3.6.b and 3.7.b the mesh structure where y^+ value 1 was selected.

3.2.2 Physical Setups

3.2.2.1 Boundary Conditions

The flow area modeled in three dimensions was influenced by atmospheric pressure and gravity as operating conditions. The symmetry condition resulting from the co-direction of the flow and the vehicle was provided to model half of the flow domain. Thus, the number of mesh created is less. Shorter analysis time, less processor and memory usage were achieved.

Inlet and outlet boundary condition were set to "velocity inlet" and "pressure outlet" respectively. Surfaces other than the symmetry plane were set to zero roughness, stationary and no-slip wall. Similarly, vehicle surfaces were also set as walls. The schematic presentation of boundary conditions were demonstrated with Figure 3.10.

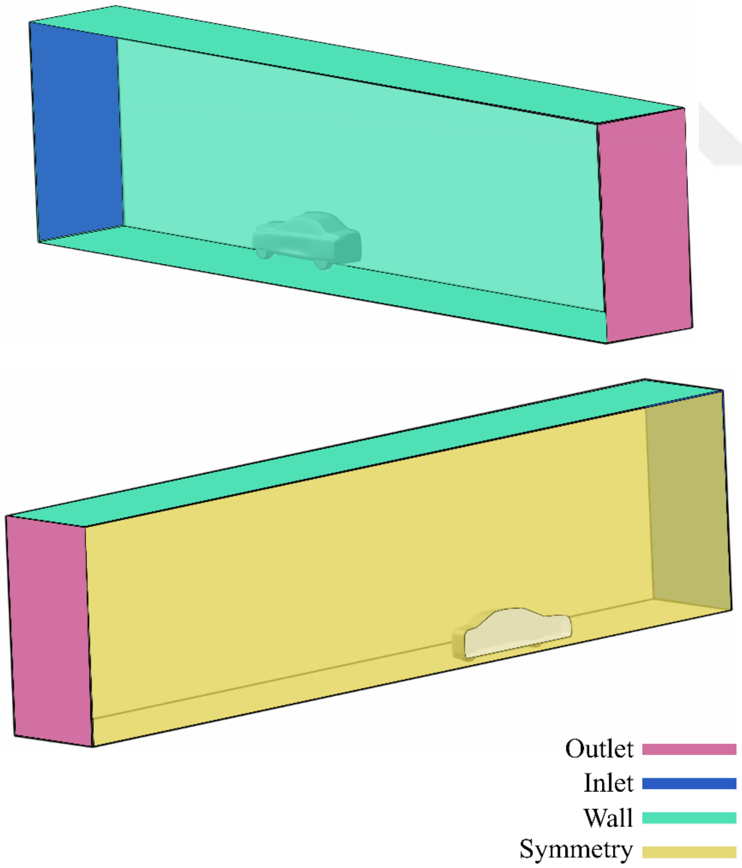

Figure 3.10 The boundary condition of flow domain

3.2.2.2 Reference Values

Specifically, values such as density, viscosity, projection area and velocity in the equations used for the calculation of dimensionless numbers such as resistance and lift coefficients are specified as reference values in ANSYS Fluent interface.

Table 3.3 Reference values of Vehicle A and B

Parameter Name	Vehicle A	Vehicle B
Projected Area [m^2]	0.0016	0.0028
Density [kg/m^3]	1.225	1.225
Dynamic Viscosity [kg/ms]	1.79E-05	1.79E-05
Freestream Velocity [m/s]	Variable	Variable

3.2.2.3 Solver and Discretization Settings

The details of the solution method and discretization scheme are as follows.

- Double precision was used for extra digits after decimal point
- Pressure based solver
- Steady-state condition
- COUPLED algorithm was selected for Pressure-Velocity Coupling scheme
- The residual values were set to 10^{-4} as the convergence criteria. Also, analyzes were continued until significant coefficients such as drag and lift coefficient were not oscillated.

CHAPTER FOUR
EXPERIMENTAL STUDY

'The universe is stamped with the adornment of harmonic proportions, but harmonies must accommodate experience.' These words were mentioned in the Cosmos, written by Carl Sagan (Sagan, 1980).

Convergence and rounding errors in the results obtained from numerical analyzes require experimental validation of these analyzes. Experimental studies are one of the most widely preferred methods in scientific research from the past to the present. In this section, the aerodynamic characteristics of the flow around the Vehicle A and B were investigated experimentally with Particle Image Velocimetry to compare with the results of numerical analysis. The findings figured out from these experimental studies were compared with the accuracy of the results obtained from the computational environment.

4.1 Flow Measurement Methods

4.1.1. Conventional Measurement Methods

Measurement of velocities or flow rates of fluids are critical for the study of various processes in the industry and experiments in laboratories. In this sense, various measurement methods with different advantages and disadvantages have been developed over time. Various flow measurement methods, which are used conventionally, are as shown in Figure 4.1.

All flowmeters in Figure 4.1 operating under different assumptions can measure with the effect of continuity principle. However, the results obtained by using these methods are insufficient because of intrusive effects on the flow domain and not examining the development characteristics of the flow.

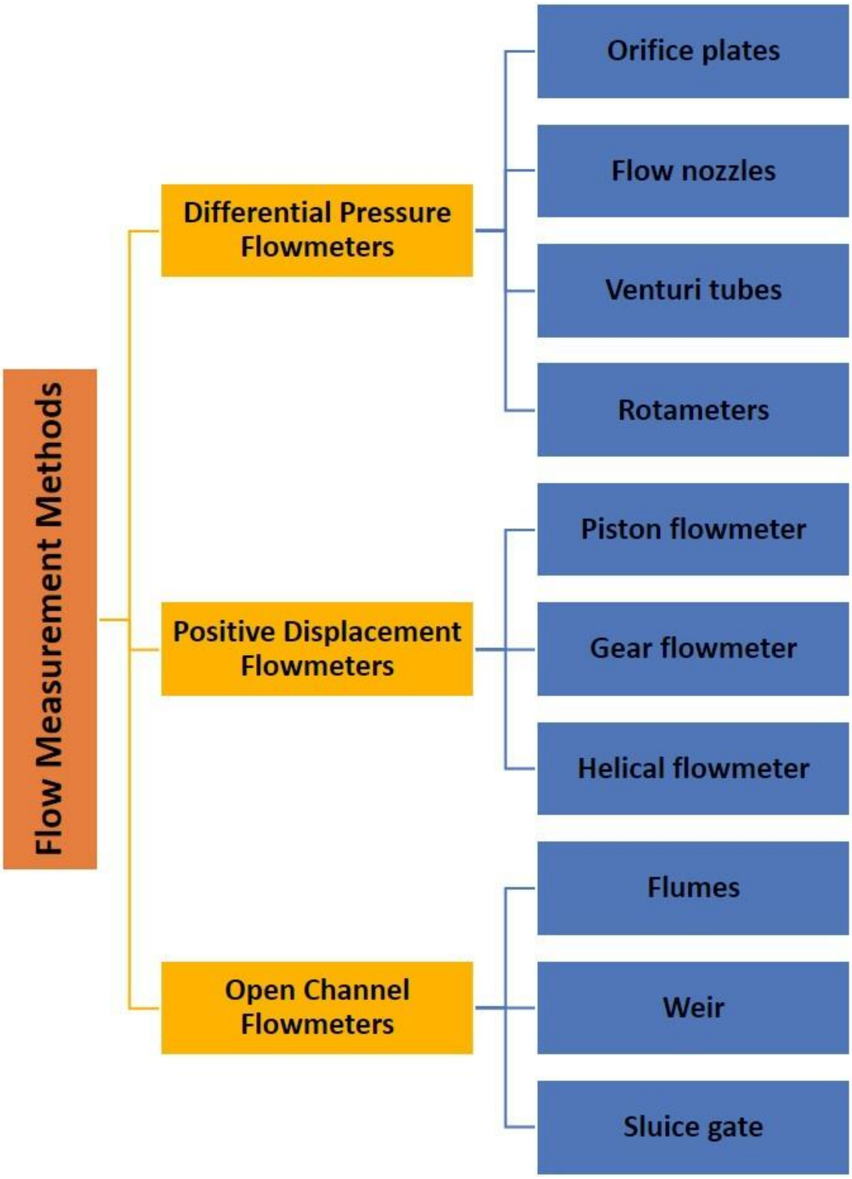

Figure 4.1 Conventional flow measurement methods

4.1.2 Hot Wire Anemometer

The hot wire anemometer (HWA) is used to measure the flow velocity of liquids and is now the most common type of sensor used in this field. The system is quite simple and small. A wire, which is heated by passing electrical current through it, is positioned against the flow direction of the liquid and the flow rate is determined. During the measurement, the heat energy lost by the wire during transport (where the temperature of the wire is higher than the fluid temperature) is equaled to the electrical energy generated by the current on the wire.

Anemometer wire is made of tungsten-platinum or platinum-iridium alloy. Its length is generally not more than 1 millimeter and its diameter is between 4 and 10 micrometer as demonstrated in the Figure 4.2. The hot wire anemometer can be used for flow rates between 0.1 m/s and 5 m/s can be measured.

Figure 4.2 The probe using in the HWA (Dantec Dynamics, 2018)

4.1.3 Laser Doppler Anemometer

Laser Doppler Anemometer (LDA) is an optical measurement method, which does not interfere to flow domain with probes, working by the principle of Doppler Effect. In this method, the tracer particles are used to observe flow. In this sense, it is very important that the selected particles are compatible with the flow. In the LDA method, the beam emitted by a special laser probe is calibrated to the point where the velocity measurement is planned as illustrated in the Figure 4.3. When the particles pass through the measurement area, they reflect the laser beam with the Doppler Effect and these beams are collected with photoreceptors. These accumulated images are processed instantly on the computer. The most important disadvantage of this system is that it measures velocity just in a single point (https://www.dantecdynamics.com, 2018).

At this point, it is necessary to explain the Doppler Effect. Doppler Effect is a physics issue based on observer-observed relationship in mechanical and electromagnetic waves. This effect is the case of any physical entity, having wave characteristics, where the frequency and wavelength are perceived differently by the approaching and moving away observer.

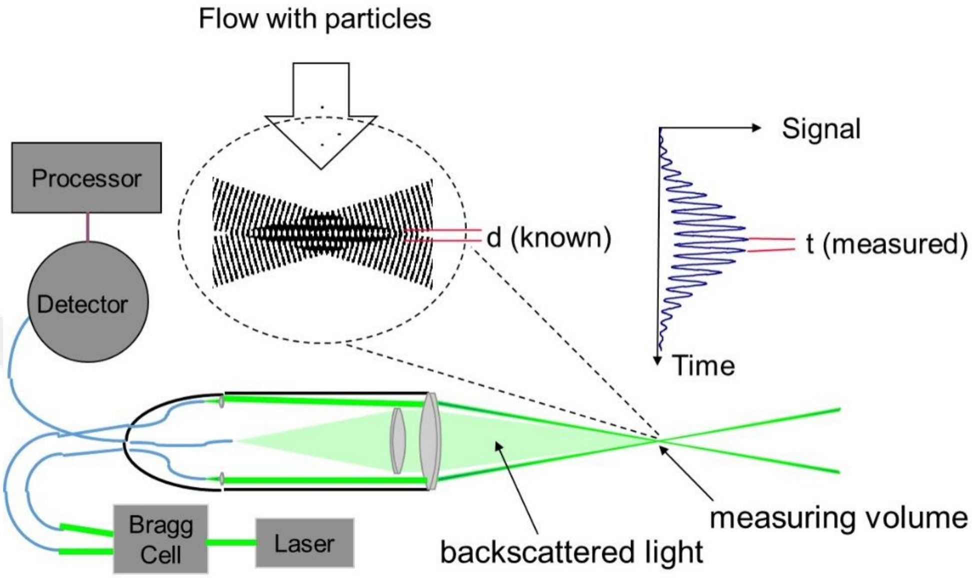

Figure 4.3 Schematic of LDA (Dantec Dynamics, 2018)

4.2 Particle Image Velocimetry (PIV)

In order to understand detailed flow structure, it is crucial to examine the formation and progression of the flow very well. However, it is impossible to see the streamlines formed around the body in a colorless or homogeneous environment such as air and water. For this reason, the streamlines in homogeneous media must be marked to observe. This situation led to spread and get advanced of flow visualization techniques. Unlike probe type measurements, in the methods where the flow is visualized with optic technique, it is great advantage that the fluid domain is not disturbed.

Two different principles are used to make the flow visible. The first one is to visualize the flow area using particles, which are coherent with the flow. Smoke or fog is added in the air and gas flow, while the flow of liquids uses gas bubbles, small aluminum and polystyrene particles. Particle Image Velocimetry is based on first visualization method. The second method such as Interferometer and Schlieren is based on the change in the optical properties of the fluid during flow. For example, when the density or temperature of the fluid changes, the refractive index changes. The cameras can image this change and these images are processed in the computer.

4.2.1 Principle of PIV

The fluid to which the particles are added flows through the experimental setup and passes through the observation zone. The observation zone is illuminated at least twice at very short intervals using the laser. Cameras working simultaneously with the laser capture the image of the particles. The resulting image pairs are then processed in the computer to obtain velocity vectors. Thus, qualitative and quantitative data about the flow area are obtained (Raffel, Willert, Wereley & Kompenhans, 2007). The schematic illustration of PIV can be seen in the Figure 4.4.

The velocity components of the fluid are obtained from two sequential images taken from the laser-illuminated surface. With one camera, two velocity components can be calculated from one surface and the third velocity component can be calculated by using a second camera.

Since this method is an optical, it is non- intrusive and is more advantageous than the methods that interfere with the flow such as HWA. In addition, it is more useful than LDA method with overall plane measurement techniques. The measured velocity value belongs to the particle, thus providing data from the flow zone indirectly. In this sense, the added particles should be small enough to be able to follow the main flow. In addition, these particles must be big enough to be visualized. Illumination whipstitch should be enough to take an instantaneous image of the flow. The duration between the two illuminations must be long enough that the movement of the particles can be examined in the image and short enough not to allow the particles to move out of the flow area. In addition, the particle density in the domain in which the PIV experiments are to be performed should be kept average (Raffel, Willert, Wereley & Kompenhans, 2007).

In this study, double pulsed ND: YAG laser with 532 nm wavelength for illumination and 4 MPx square sensor cameras for imaging were used. The interrogation area used for the creation of velocity vectors was set to 32 * 32 pixels and the overlap ratio was set to 50%.

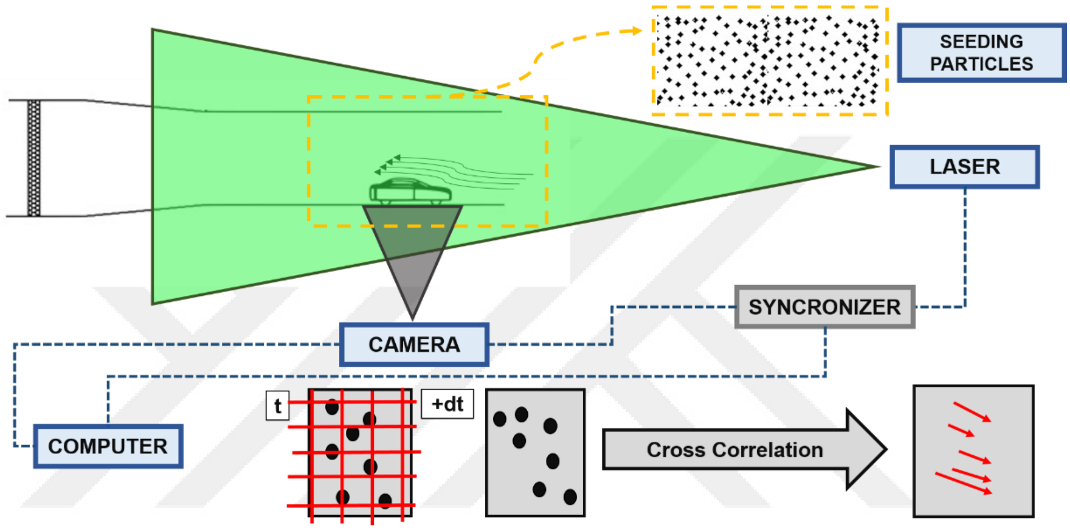

Figure 4.4 Principle of the PIV methodology

4.2.2 Components of the PIV Setups

The components that must be in a PIV setup are as shown in the Figure 4.5. There are five basic components including laser, camera & lens, synchronizer, fog generator and computer. The functions of these components in the setup are as described previous section.

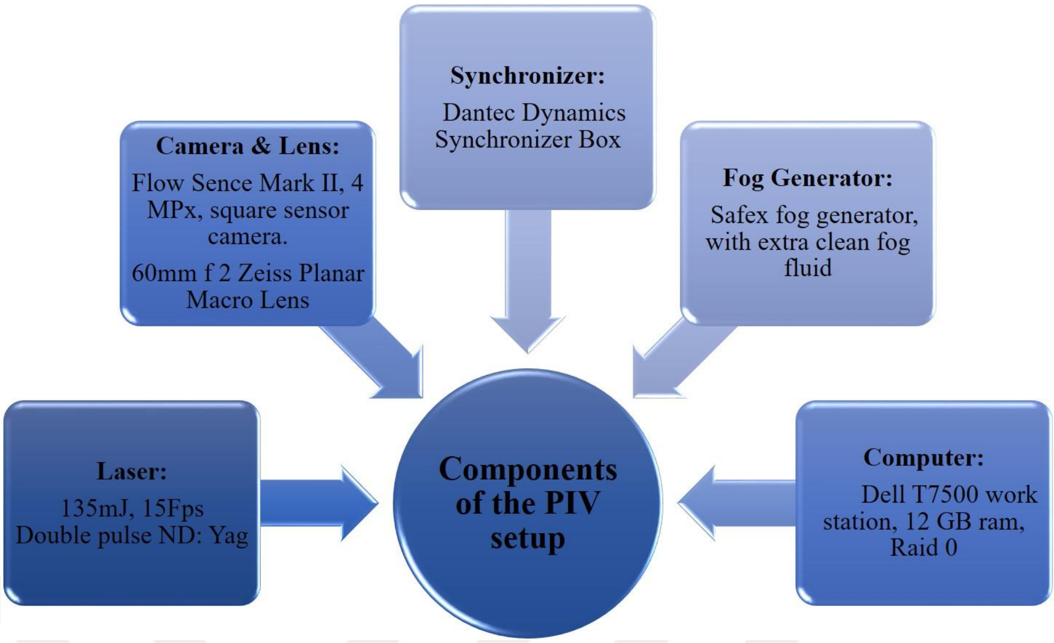

Figure 4.5. Components of the PIV setups

4.2.2.1 Laser

Laser is an electronic element that provides a very high level of illumination used as a source of light that particles must reflect. The laser in this study is the solid state ND: YAG laser produced by using crystal named as Neodymium-Doped Yttrium Aluminum Garnet. The ND: YAG laser produces a wavelength of 1064 nm, which is in the infrared range. Therefore, two pulses are generated which are half of the total wavelength by using double oscillator system. The current laser, used in this study is as shown in the Figure 4.6.

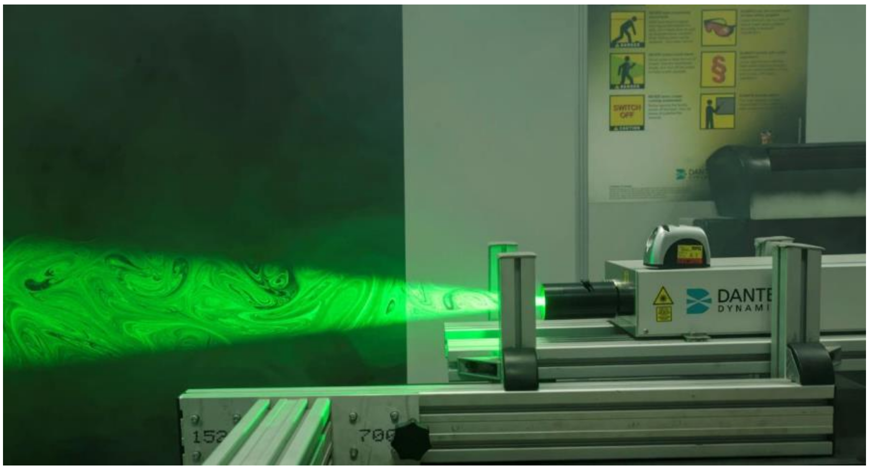

Figure 4.6 The photo of the current laser (Özer, 2017)

4.2.2.2 Cameras and Lenses

High-speed cameras must take the image of particles which reflecting the light provided by the laser. In this sense, PIV cameras are designed with CCD (Charge Coupled Device) or CMOS (Complementary Metal-Oxide Semi-Conductor) sensors. The images taken by the PIV cameras are very important in the accurate construction of vector maps. The cameras used in this study are as shown in the Figure 4.7.

Figure 4.7 Current cameras in the PIV setup (Özer, 2017)

4.2.2.3 Synchronizer

This device works for the camera and laser as an external trigger. In order to get a smooth image, it is necessary to have the image recording and lighting simultaneously. Otherwise, photos appear black with no illumination and the particles cannot be observed.

4.2.2.4 Fog Generator (Seeding particles)

Seeding is the process of incorporating particles that are capable of reflecting light, to the flow. These particles act together with the flow to provide visualization and resolution of flow components. PIV setup requires some features for these particles to achieve experimental accuracy as illustrated in the Figure 4.8. In addition, current seeder used in this study is as shown in the Figure 4.9.

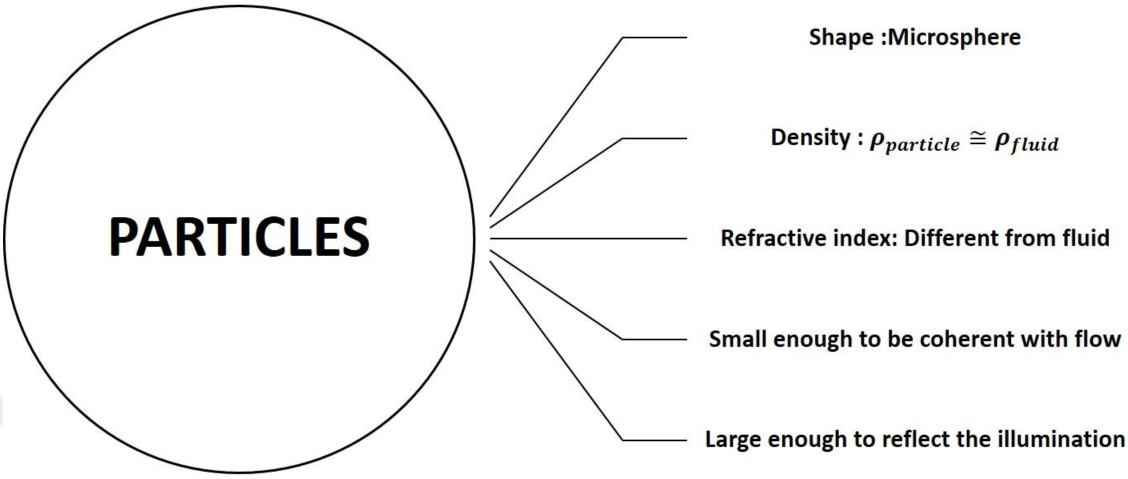

Figure 4.8 Features for particles in PIV

Figure 4.9 Photo of seed generator used in this study (Özer, 2017)

4.2.2.5 Computer and Software

After all the steps mentioned above, images taken into computer environment are divided into interrogation areas. The cross-correlation between these formed interrogation areas enables the creation of vector maps. As a result of the cross-correlation, the maximum similarity between the interrogation domains determines the starting and ending points of the vector. The basic principle of cross-correlation is as shown in the Figure 4.10.

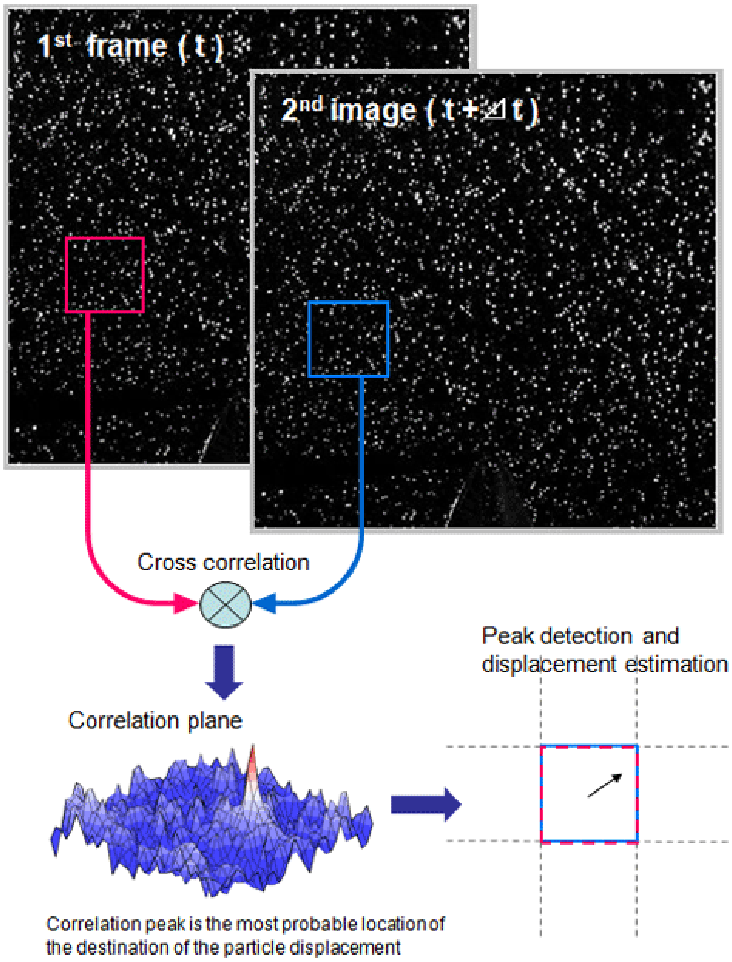

Figure 4.10 Basic principle of cross- correlation (Seika, 2018)

4.3 The Design of Flow Domain

The flow domain design to be examined by PIV experiments was carried out in two stages. First, the geometry of the vehicle was created. After that, the tunnel geometry where the vehicle is placed was designed.

4.3.1 The Design of Vehicle Model

The product, which was designed as two different body by scaled it by 1/24, was printed using 3D printer. The 3D printer used in this study was given in the Figure 4.11.a. schematic of this 3D printer was illustrated with Figure 4.11.b.

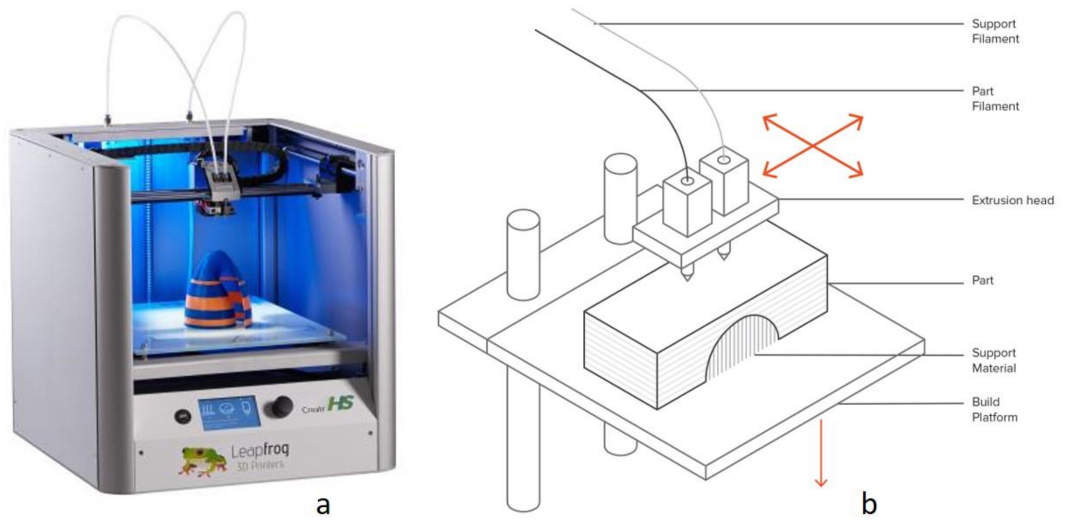

Figure 4.11. a. 3D printer used in this study b. Schematic illustration of this 3D printer (LeapFrog, 2018)

The fact that the vehicle geometry was printed in two sub-geometries is to minimize the error rate due to the thermal distortion. The printed geometry is as shown in the Figure 4.12.

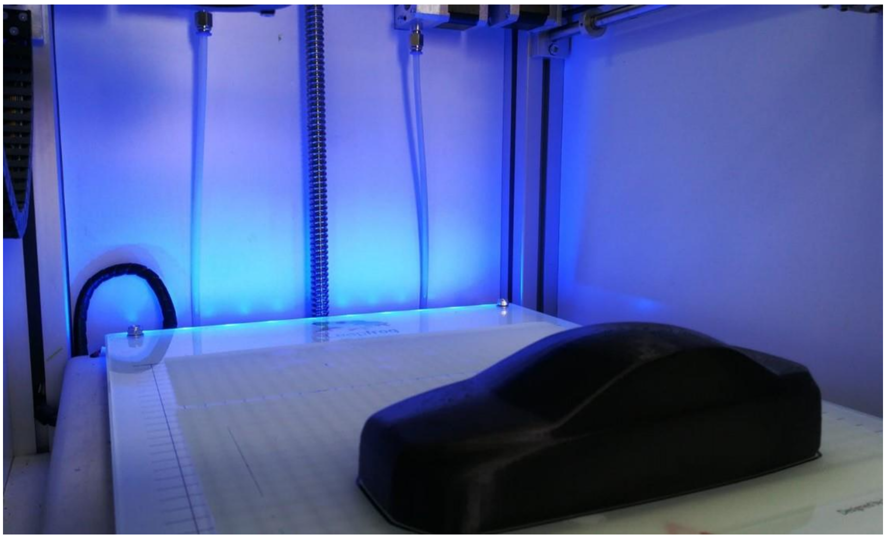

Figure 4.12 Printed vehicle geometry (Personal archive, 2019)

After the printing process, both bodies were sandpapered to obtain smooth surfaces. These two sub-geometries and preparation stages were given in Figure 4.13. The parts that were prepared as surface quality were glued and the vehicle preparation stages were completed.

Figure 4.13 Sub-geometries of the vehicle (Personal archive, 2019)

4.3.2 The Design of Wind Tunnel

The wind tunnel, which was designed with the limitations of the existing test chamber and PIV mechanism, works with air pumping as opposed to the tunnels currently used. The tunnel consists of three basic parts: the fan domain, the constriction domain and the observing domain.

This region was produced by using Plexiglas to ensure laser transition and to prevent camera vision. When calculating the geometric dimensions of the region, the blockage ratio of the vehicle in the flow domain was taken into consideration. The blockage rate is obtained by dividing the projective area of the vehicle by the cross-sectional flow area and it is stated that it should be less than 7.5% in the literature. The maximum blockage rate of the channel and vehicle geometry designed in this study was calculated as 0.046. The blockage of the designed vehicle geometry in the flow area is as shown in the Figure 4.14.

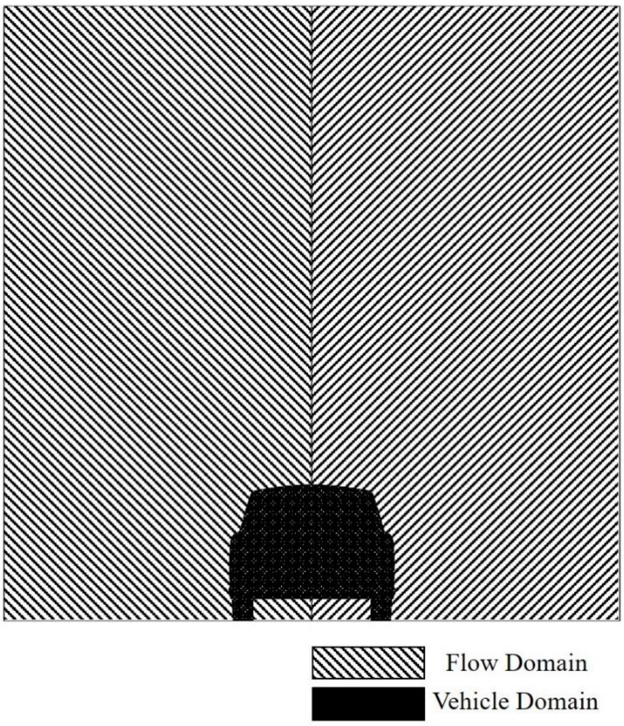

Figure 4.14 Blockage of the vehicle formed in flow domain

Within the scope of the experiments, the flow region geometry specified in the numerical study was used. The image of Vehicle B captured during the PIV experiments is given in Figure 4.15.

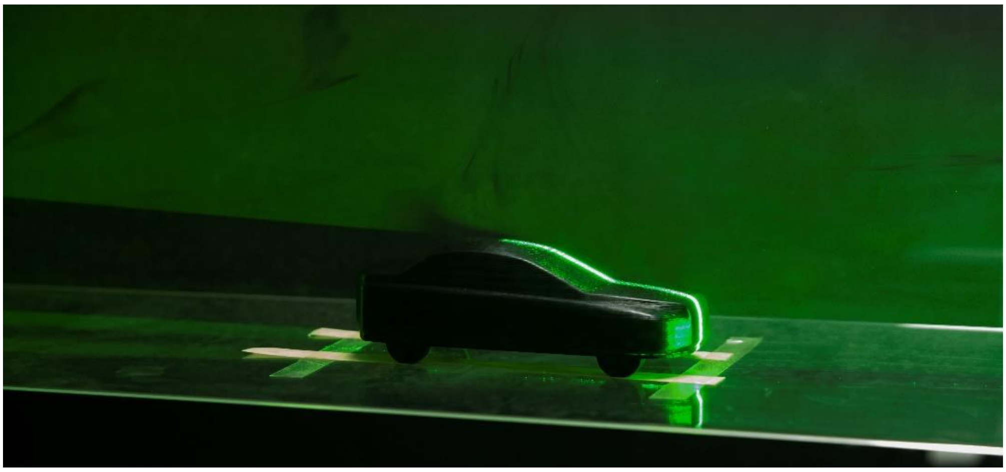

Figure 4.15 Image of Vehicle B captured during the PIV experiments (Personal archive, 2019)

CHAPTER FIVE
RESULTS AND DISCUSSION

5.1 Experimental Validation

First, velocity map and contour graphs obtained with Particle Image Velocimetry (PIV) experiments in wind tunnel where free steam velocity reached 24 m/s were compared with numerical analysis results. In the numerical analysis to be compared with PIV results, 24 m/s inlet velocity, realizable k-ε turbulence model (with mesh structure Figure 3.7.a - higher y+) and Vehicle B were used. The results obtained with PIV experiments were given in Figure 5.1 for a velocity value of 24 m/s.

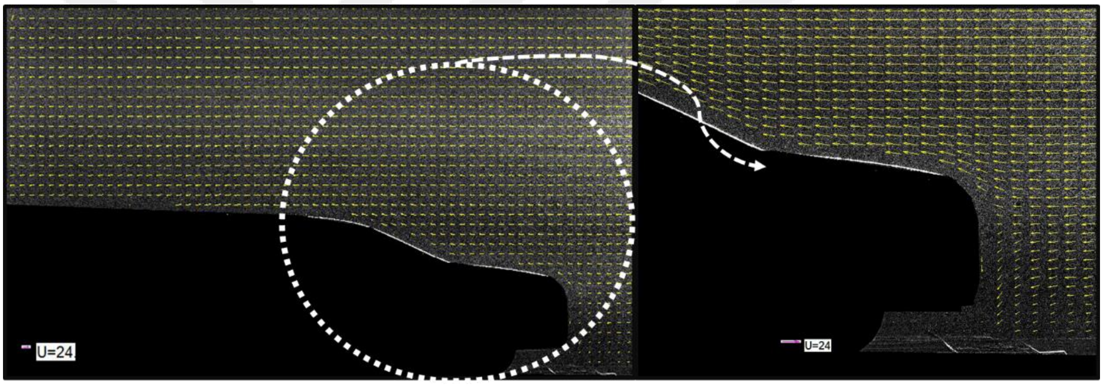

Figure 5.1 Velocity map obtained from PIV (Günay et al., 2019)

In Figure 5.1, it was seen that the flow which separated in the front nose of the vehicle was reached its maximum value by following the upper body. At the top of the vehicle, the velocity was reached approximately 30 m/s with the constricting channel effect.

In addition, the numerical results in terms of velocity map with the same conditions as PIV setup were given in Figure 5.2. When Figure 5.2 was examined, it was seen that flow separations were formed in the same way. When the results of both studies were compared in terms of the obtained velocity values, a difference of 4.8% was found (Günay et al., 2019).

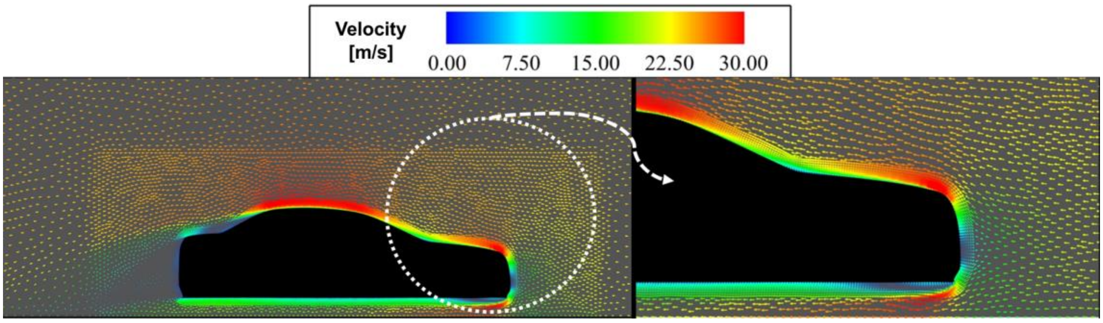

Figure 5.2 Velocity map obtained from CFD (Günay et al., 2019)

5.2 Results of Numerical Analyzes

Based on the validation status, the analyzes were repeated for different velocity values, geometries, mesh structures (y^+ value) and turbulence models. The results were compared in terms of flow separations, velocity maps and aerodynamic resistance (represented with the multiplication of C_D and A, C_D*A).

The velocity contour graphs of different setups was shown in the Figure 5.3. These results were obtained by using 20 m/s with realizable k-ε and SST k-ω inlet velocity for Vehicle A and B. When the Figure 5.3 was interpreted, it was seen that the minimum velocity zones formed in the rear regions (wake region) of two different vehicles developed differently. It was seen that different turbulence models affect the velocity development profile on the vehicle. Considering the velocity graph of Vehicle A, a more detailed solution was obtained with the SST k-ω model, especially in the back of the vehicle. In this sense, it can be concluded that the mesh structure created with low y+ values provides more detailed results in boundary layer solutions. The same solution sensitivity status was also observed for Vehicle B.

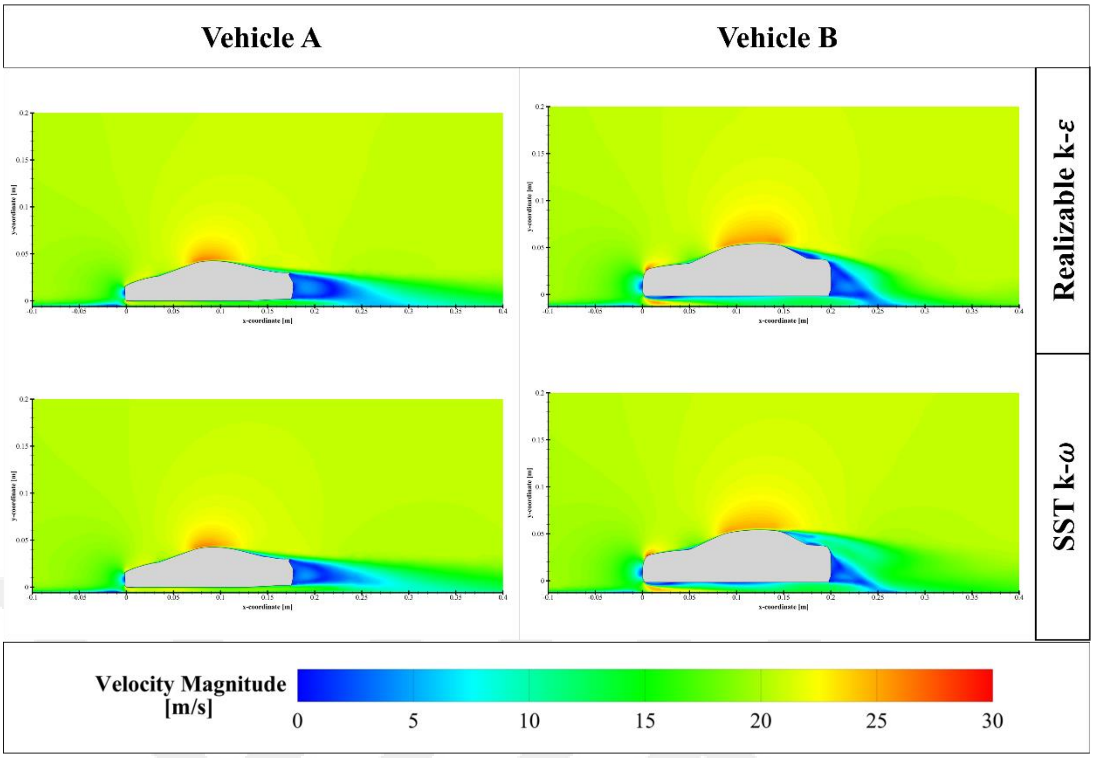

Figure 5.3 Velocity contours obtained from different setups (V_{inlet}= 20 m/s)

The analyzes were repeated for velocities of 30 m/s and 25 m/s. The results were compared with a velocity of 20 m/s. The result for 30 m/s velocity inlet was given with Figure 5.4. The velocity graphs showed that for the analysis with 30 m/s, the low velocity field on the rear region of the vehicles was higher.

In addition, aerodynamic resistance values were calculated for repeated analyzes. The comparison of Vehicle A and B for 3 velocities and 2 turbulence models was given in the Table 5.1. When the values of Table 5.1 were examined, it was seen that there was less aerodynamic drag for Vehicle A compared to Vehicle B. In view of this situation, a greater aerodynamic resistance of the Vehicle B, which created a greater blocking rate in the flow domain and which was more suitable for flow separation due to its rear geometry, was formed.

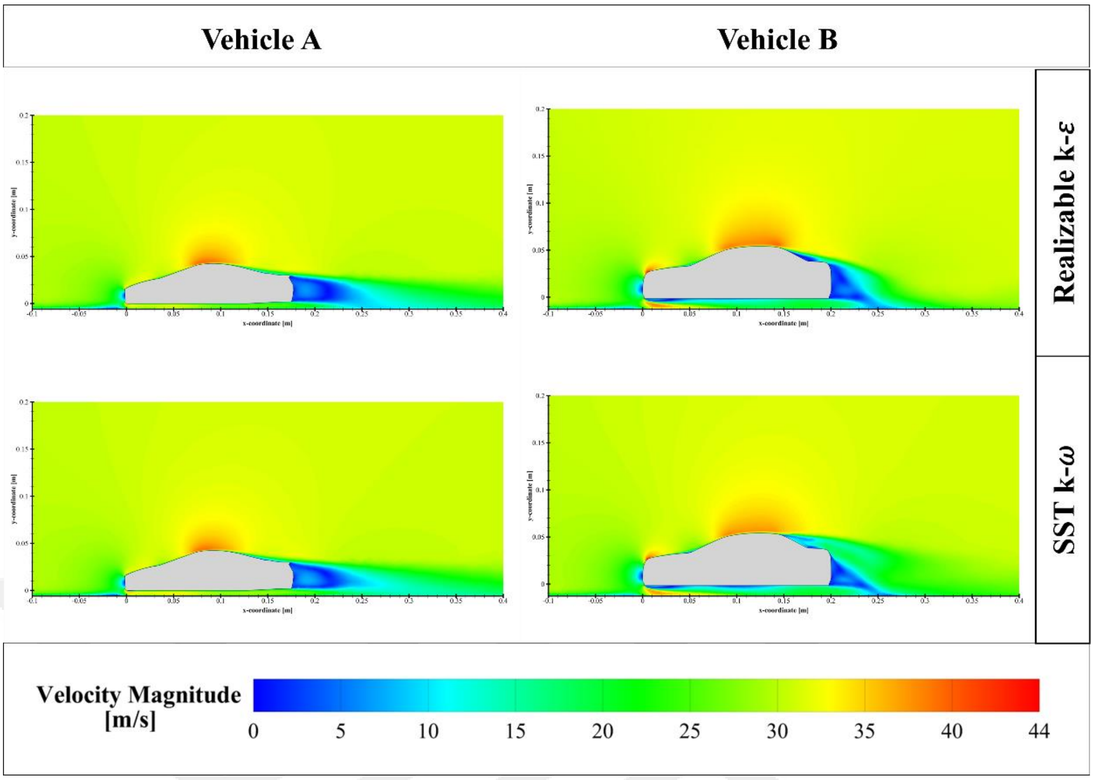

Figure 5.4 The velocity contours obtained from different setups (V_{inlet} =30 m/s)

Table 5.1 Aerodynamic resistances of Vehicle A and B for different turbulence models and velocities

Turbulence Model		**Realizable k- ε**			**SST k-w**		
Velocity [m/s]		**20**	**25**	**30**	**20**	**25**	**30**
C_D * A (10^{-3})	**Vehicle A**	0.8510	0.8271	0.8240	0.8372	0.8059	0.7969
	Vehicle B	1.7143	1.6770	1.6755	1.8640	1.8403	1.8445

Moreover, the aerodynamic resistance of the vehicles decreases as the wind speed increases. The different resistance coefficients obtained for the same velocity and geometry were resulted from the solution capacities of the different turbulence models on the velocity boundary layer. In addition, the aerodynamic forces acting on the Vehicle A and B were shown in the Figure 5.5 for three velocity values and 2 turbulence models. When the graph was examined, it was seen that the increasing velocity values, acting on the vehicles, was increased the aerodynamic forces. Differences in aerodynamic resistances observed for different turbulence values were found to be valid within aerodynamic forces.

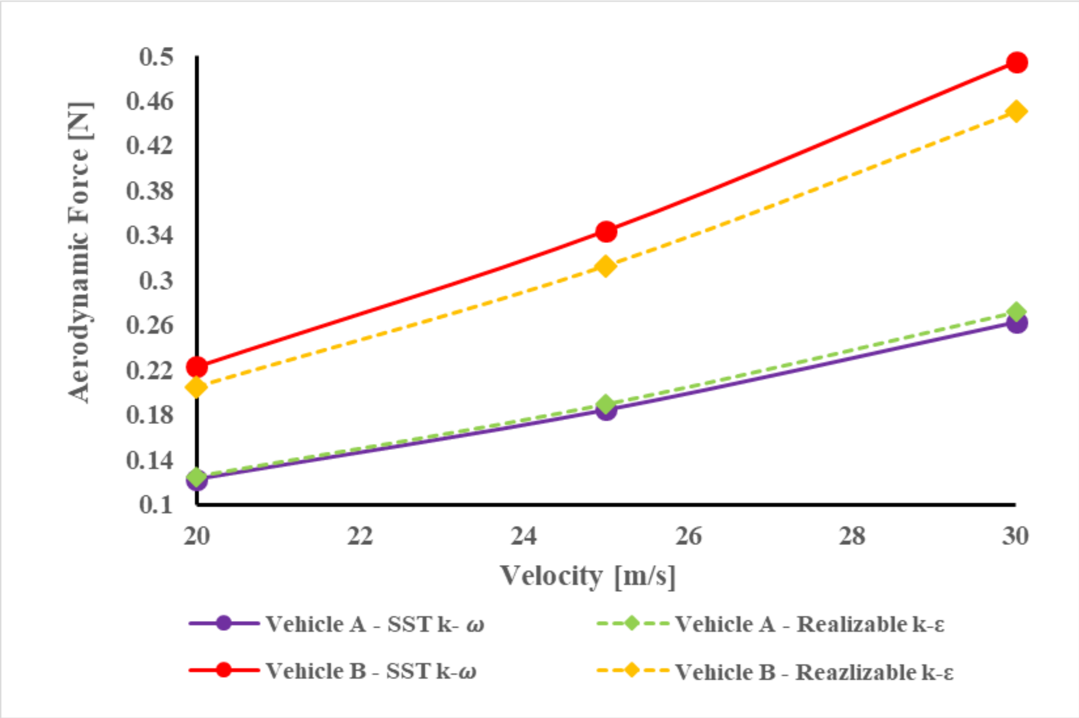

Figure 5.5 The effect of velocity and turbulence model on the aerodynamic force

CHAPTER SIX
CONCLUSION

In this study, the aerodynamic effect of two vehicle geometries with different front and rear designs on the velocity distributions around the vehicle was investigated by Computational Fluid Dynamics. Particle Image Velocimetry method was applied inside of a scaled wind tunnel for the validation of these results. When the results of both studies were compared in terms of the obtained velocity values, a difference of 4.8% was found. Based on the validation status, the analyzes were repeated for three velocity values, two geometries, two mesh structures (y^+ value) and two turbulence models. Considering the velocity graph of Vehicle A, a more detailed solution was obtained with the SST k- ω model, especially in the back of the vehicle. In this sense, it can be concluded that the mesh structure created with low y^+ values provides more detailed results in boundary layer solutions. In addition, the results of the analysis for three velocity and two turbulence models showed that the Vehicle B had greater aerodynamic drag than A. The different resistance coefficients obtained for the same velocity and geometry were resulted from the solution capacities of the different turbulence models on the velocity boundary layer. According the coherence between the PIV experiments and the numerical analysis, the methodology was also established for other designs where aerodynamic characteristics were effective.

REFERENCES

Adrian, R. J. (2005). Twenty years of particle image velocimetry. *Experiments in Fluids*, *39*, 159-169.

Ahmed, S.R., Ramm, G., Faltin, G. (1984). Some salient features of the time-averaged ground vehicle wake. *SAE Transaction*, 473-503.

Basic, J. (2016). *Turbulent history of fluid mechanics (brief essay)*. Retrieved November 25, 2018, from https://sci-hub.tw/https:// www.researchgate.net/publication/291821947_Turbulent_history_of_fluid_mechanics_brief_essay

Bernard Go Mars. (2013). Retrieved November 25, 2018, from https: //commons.wikimedia.org/wiki/File: Canal_hydraulique_de_Prandtl_1904.png

Buchheim, R., Deutenbach, K., & Lückoff, H. (1981). Necessity and premises for reducing the aerodynamic drag of future passenger cars. *SAE Transactions*, *90*, 758-771.

Buresti, G. (2000). *Bluff body aerodynamics. Department of Aerospace Engineering*, Lecture Notes, University of Pisa, Italy.

Cengel, Y. A. & Cimbala, J. M. (2006). Fluid Mechanics: *Fundamentals and applications* (First Edition). New York, NY: McGraw-Hill.

Dantec Dynamics (n.d). Retrieved November 25, 2018. https://www.dantecdynamics.com/

Desai, M., Channiwala, S. A. & Nagarsheth, H.J. Experimental and computational aerodynamic investigations of a car. *WSEAS Transactions on Fluid Mechanics, 4*(3), 359-368.

Depardon, S., Lasserre, J. J., Boueilh, J.C., Brizzi, L. E. & Boree, J. (2005). Skin friction pattern analysis using near-wall PIV. *Experiments in Fluids*, *39*, 805–818.

Depardon, S., Lasserre, J. J., Brizzi, L. E. & Boree, J. (2006). 1/4 scale vehicle wake pattern analysis using Near-Wall PIV. *Journal of Passenger Car: Mechanical Systems Journal*, *115*(6), 966-978.

Guilmineau, E. (2008). Computational study of flow around a simplified car body. *Journal of Wind Engineering and Industrial Aerodynamics*, *96*(6-7), 1207-1217.

Gurlek, C., Sahin, B. & Ozkan, G. M. (2012). PIV studies around a bus model. *Experimental Thermal and Fluid Science*, *38*, 115–126.

Hetawala, S., Gophaneb, M., Ajay, B.K. & Mukkamalad, Y. (2014). Aerodynamic study of Formula SAE Car. *Procedia Engineering*, *97*, 1198 – 1207.

Hucho, W.H. (1986). *Aerodynamics of road vehicles from fluid mechanics to vehicle engineering* (First Ed.). Oxford: Butterworth-Heineman.

Hucho, W.-H., Janssen, L.J. & Emmelmann, H.-J. (1976). The optimization of body details—A method for reducing the aerodynamic drag of vehicles. *SAE Transactions*, 760-185.

Kim, J. S., Kim, S., Sung, J., Kim, J.D. & Choi, J. (2006). Effects of an air spoiler on the wake of a road vehicle by PIV Measurements. *Journal of Visualization*, *9*(4), 411- 418.

Koike, M., Nagayoshi, T. and Hamamoto, N., (2004), Research on aerodynamic drag reduction by vortex generators. *Mitsubishi Motors Technical Review*, (16), 11-16.

Kost F. (2014). Basic principles of vehicle dynamics. In: Reif K. (eds) Fundamentals of Automotive and Engine Technology. *Bosch Professional Automotive Information*, (114 – 129). Wiesbaden: Springer.

Lienhart, H., & Becker, S. (2003). Flow and turbulence structure in the wake of a simplified car model. *SAE Transactions*, *112*, 785-796.

McCutcheon, G., McColgan, A. H., Grant, I. & Hurst, D. Wake studies of a model passenger car using PIV. S*AE Motorsports Engineering Conference and Exhibition*, 382-393.

Modi, V.J., Hill, S.S. & Yokomizo, T. (1995). Drag reduction of trucks through boundary-layer control. *Journal of Wind Engineering and Industrial Aerodynamics 54*/55, 583-594.

Nayeri, C.N., Wieser, D., Schmidt, H-J., Strangfeld, C. & Paschereit, O. (2014). Experiments on the influence of yaw on the aerodynamic behaviour of realistic car geometries. *International Vehicle Aerodynamics Conference,* (43-51).

Ozawa, H., Nishikawa, S. & Higashida, D. (1998). Development of aerodynamics for a Solar Race Car, *SAE Review 19*(4), 343-349.

Ozer, Ö. (2017). *Investigation of fan driven flow fields by particle image velocimetry and infrared thermography*. Ph. D. Thesis, Dokuz Eylül University, Izmir.

Parab, A., Sakarwala, A., Paste, B., Patil, V. & Mangrulkar, A. (2014). Aerodynamic analysis of a car model using ANSYS- Fluent 14.5. *International Journal on Recent Technologies in Mechanical and Electrical Engineering (IJRMEE), 1*(4), 7-13.

Raffel, M., Willert, C., Wereley, S. & Kompenhans, J., (2007). *Particle image velocimetry a practical guide* (2nd Ed.). New York: Springer.

Rajsinh B. C. & Raj T. K. R. (2012). Numerical investigation of external flow around the Ahmed reference body using Computational Fluid Dynamics. *Research Journal of Recent Sciences*, *1*(9), 1-5.

Sims-Williams, D. & Dominy, R., (1998). Experimental investigation into unsteadiness and instability in passenger car aerodynamics. *SAE Technical Paper*, 980391.

Song, K.S., Kang, S. O., Jun, S.O., Park, H. I., Kee, J. D., Kim, K. H., & Lee, D.H. Aerodynamic design optimization of rear body shapes of a sedan for drag reduction. *International Journal of Automotive Technology*, *13*(6), 905−914

Spohn A. & Gillieron P. (2002). Flow separations generated by a simplified geometry of an automotive vehicle. *In IUTAM Symposium: Unsteady Separated Flows*, April 8-12.

Suzuki, M., Tanemoto, K. & Maeda, T. (2003). Aerodynamic characteristics of train/vehicles under cross winds. *Journal of Wind Engineering and Industrial Aerodynamics*, *91*, 209-218.

Watkins, S. & Vino, G. (2008). The effect of vehicle spacing on the aerodynamics of a representative car shape, *Journal of Wind Engineering and Industrial Aerodynamics*, *96*, (6–7), 1232-1239.

Windsor S. (2014). Real world drag coefficient – is it wind averaged drag? *International Vehicle Aerodynamics Conference*, 3-13.